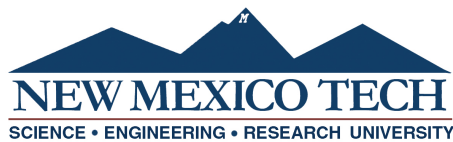


**PLUME IDENTIFICATION AND ANALYSIS
USING SCHLIEREN AND BACKGROUND ORIENTED
SCHLIEREN**

by

Maria N. D'Orazio

Submitted in Partial Fulfillment
of the Requirements for the Degree of
Master of Science in Mechanical Engineering
with Specialization in Explosives Engineering



New Mexico Institute of Mining and Technology
Socorro, New Mexico
May, 2025

This thesis is dedicated to Dom, Kat, and Dennis, who have always spurred me to be the best version of myself.

Maria N. D'Orazio
New Mexico Institute of Mining and Technology
May, 2025

ACKNOWLEDGMENTS

I want to thank my advisor, Dr. Michael Hargather, and all of the friends that I made at the SGDL for showing me the joys of research. I want to thank all of my friends for their unending love and encouragement, and my parents for all they do.

Funding for this work by DOE/NNSA MSIPP award DE-NA0004108, and the U.S. Department of Energy's Office of Energy Efficiency and Renewable Energy (EERE) under the BENEFIT program with award number DE-EE0010914.

This thesis was typeset with \LaTeX ¹ by the author.

¹The \LaTeX document preparation system was developed by Leslie Lamport as a special version of Donald Knuth's \TeX program for computer typesetting. \TeX is a trademark of the American Mathematical Society. The \LaTeX macro package for the New Mexico Institute of Mining and Technology thesis format was written by John W. Shipman.

ABSTRACT

Helium plumes in air were imaged using lens-type schlieren and shadowgraph, and background oriented schlieren (BOS) to observe plume behavior as a function of Reynolds number. Helium plumes in lens-type schlieren systems were imaged with horizontal cutoff, vertical cutoff, and circular cutoff, along with focused and de-focused shadowgraphy in order to analyze the plume edge behavior in laminar, turbulent, and transitional regimes with jet Reynolds numbers ranging from 200 to 2980. Fractal dimension was correlated to the jet Reynolds number by performing box counting on isolated plume edges. BOS images were taken using projected, laser speckle, and printed backgrounds to compare the quality of BOS visualization of the plumes. Six different BOS sensitivities characterized by the b/L length ratio were tested for each of the three background types in order to determine at what background distance resolution was lost for BOS systems. All BOS images were processed using both Horn-Schunck optical flow and wavelet based optical flow analysis (wOFA). It was determined that wOFA was the most effective method of optical flow for all background and b/L combinations. The methods explored here enable characterization of plumes and the ability to detect plumes in non-ideal BOS imaging configurations for applications such as evaluating building envelope efficiency.

Keywords: schlieren; background oriented schlieren; plume detection; optical flow; sensitivity limits; fractal dimension

CONTENTS

	Page
LIST OF TABLES	vii
LIST OF FIGURES	viii
LIST OF ABBREVIATIONS	xii
CHAPTER 1. INTRODUCTION	1
1.1 Research Motivation	1
1.2 Refractive Imaging Techniques	2
1.2.1 Schlieren	2
1.2.2 Shadowgraphy	3
1.2.3 Background Oriented Schlieren	5
1.3 Fractal Behavior and Box Counting	7
1.4 Image Processing	8
1.4.1 Optical Flow	9
1.4.2 Edge Detection Techniques	9
1.5 Research Objectives	11
CHAPTER 2. EXPERIMENTAL METHODS	12
2.1 Lens-type Schlieren and Shadowgraphy	12
2.2 Background Oriented Schlieren	17
2.2.1 BOS Processing Optical Flow Methods	21
CHAPTER 3. SCHLIEREN AND SHADOWGRAPHY PLUME DETECTION AND RESULTS	23
3.1 Edge Detection Techniques	23
3.1.1 Box-counting Methods	27
3.2 Plume Fractal Dimension	28

CHAPTER 4. LIMITS OF DETECTION FOR BOS IMAGES	33
4.1 Limits of plume detection for BOS	33
CHAPTER 5. CONCLUSIONS AND FUTURE WORK	49
5.1 Conclusions	49
5.2 Future Work	50
REFERENCES	52
APPENDIX A. CODES	56
A.1 Schlieren Edge Detection Code	56
A.2 Horn-Schunck Optical Flow Code and Functions	64
APPENDIX B. PERMISSIONS	72

LIST OF TABLES

Table	Page	
1.1	Previously published values for fractal dimension of turbulent plume edges.	8
2.1	Jet exit velocity values corresponding to individual Reynolds numbers	14
2.2	Lens $f/\#$ used for each BOS experiment	18
2.3	Pixel per mm ratio for the background at each b/L distance	20
3.1	Threshold (T) values used for the MATLAB <i>edge</i> function based on flow region, and cutoff orientation, where SG is shadowgraph . . .	24
3.2	Standard deviations of fractal dimension in 1000 image sets for select cutoffs and Reynolds numbers, as well as mean uncertainty in the linear fit to find fractal dimension for each image in the set. . .	31
4.1	Threshold (T) values used for the MATLAB <i>edge</i> function based on background type and b/L value for full plume edge detection . . .	42
4.2	Slopes of linear fit lines for each processing method and background type combination when average flow on pixel shifts are subtracted from average flow off pixel shifts	46

LIST OF FIGURES

Figure	Page
Figure 1.1 Schematic of a lens-type schlieren system	2
Figure 1.2 (a) An image of a calibration lens in a lens-type schlieren setup compared to (b) an illustration of parallel light passing through a calibration lens with focal length f , where R is the radius of the lens and r_c is the distance from the center of the lens for a given point. ϵ_R represents the maximum refraction angle at the edge of the lens, and ϵ represents the angle of refraction for radius r_c in the calibration lens.	3
Figure 1.3 Schematic of a direct shadowgraphy system, where the background is a distance L from the camera and a distance b from the refractive disturbance, and ϵ represents the angle of refraction caused by the disturbance. d_e represents the actual length of the disturbance, and d'_e represents the length of the disturbance's projection.	4
Figure 1.4 General BOS setup where L is the distance between the background and the camera, t is the distance from the camera to the refractive disturbance, b is the distance from the refractive disturbance to the background, e is the measured pixel shift, θ is the angle measured from the center line of the camera, and ϵ is the angle of refraction.	6
Figure 1.5 The same lens-type schlieren image of bubbles in the (a) spatial domain and (b) frequency domain shifted so that the lowest frequencies are in the center of the image	11
Figure 2.1 Schematic of schlieren setup used for imaging helium plumes where LS represents the light source, SL1 and SL2 are the collimating and refocusing schlieren lenses, respectively, KE represents the knife edge, and CL represents the camera lens. The shadowgraphy system is identical to the schlieren system with the knife edge removed.	13
Figure 2.2 Image of the experimental setup for schlieren and shadowgraph images of helium plumes.	13

Figure 2.3	Examples of each type of cut off for a helium plume with a Reynolds number of 1985: (a) vertical cutoff, (b) horizontal cutoff, (c) circular cutoff, (d) focused shadowgraphy, (e) de-focused shadowgraphy.	14
Figure 2.4	Vertical cutoff schlieren images representing each Reynolds number imaged: (a) 200, (b) 400, (c) 600, (d) 775, (e) 800, (f) 835, (g) 895, (h) 990, (i) 1190, (j) 1985, (k) 2580, and (l) 2980.	15
Figure 2.5	Helium plumes with a vertical cutoff representing each flow regime at Reynolds numbers of (a) 400 (laminar), (b) 800 (transitional), and (c) 2980 (turbulent).	16
Figure 2.6	Types of BOS backgrounds: (a) printed background, (b) projected background, and (c) laser speckle background.	17
Figure 2.7	Two views of the BOS setup used to image helium plumes.	18
Figure 2.8	Schematic of BOS Setup for imaging helium plumes with (a) the printed background, (b) the projected background, and (c) the laser speckle background.	19
Figure 2.9	Demonstration of the shadowgraph effect caused by the projected background at $b/L = 0.3$. The shadowgraph effect is offset down and to the right because the light was above and to the left of the camera as shown in Figure 2.8b	20
Figure 2.10	(a) Raw BOS image with $b/L = 0.4$ of helium plume with $Re = 1985$ compared to (b) the same image processed through Horn-Schunck optical flow using a flow on background image.	21
Figure 2.11	(a) Raw BOS image with $b/L = 0.4$ of helium plume with $Re = 1985$ compared to (b) the same image processed through wOFA using a flow on background image.	22
Figure 3.1	Image processing steps demonstrated for a $Re = 1985$ plume with vertical cutoff schlieren imaging: (a) background subtracted original image (b) image after high pass Gaussian filter (c) canny edge detection.	24
Figure 3.2	The raw images of a laminar, transitional, and turbulent plume imaged with vertical cutoff shown with edge only and full plume edge detection, as well as both edge detection methods overlaid on the raw image of the plume.	26
Figure 3.3	(a) A binary image of turbulent ($Re = 1985$) plume edges on which (b) box counting is visually demonstrated and a (c) plot of the log of the number of counted boxes (N_r) versus the log of one over box size in pixels ($1/r$) for the image shown.	27
Figure 3.4	Mean fractal dimension of 1000 images vs Re for each cutoff type using full plume edge detection.	29

Figure 3.5	Mean fractal dimension of 1000 images vs Re for select cut-off types using edge only edge detection.	30
Figure 3.6	Histogram distribution of fractal dimension for each flow rate in the vertical cutoff. Each flow has 1000 images processed. . .	31
Figure 3.7	Edge detection of transitional plumes with Reynolds number = 835 (a) vertical cutoff (whole image D = 1.3516) (b) de-focused shadowgraph (whole image D = 1.4182) (c) focused shadowgraph (whole image D = 1.3960) (d) Graph showing the variation of fractal dimension along the plume length.	32
Figure 4.1	Raw BOS images of each background type: (a) printed, (b) projected, and (c) laser speckle, all with a b/L value of 0.4.	34
Figure 4.2	Singular BOS images processed using Horn-Schunck optical flow for each combination of background and b/L distance, with Re = 1985.	35
Figure 4.3	Singular BOS images processed using the wOFA approach for each combination of background and b/L distance, with Re = 1985	36
Figure 4.4	Depiction of the areas averaged in each BOS image to determine average pixel shift, showing a plume imaged with a b/L of 0.4 against printed background and processed using Horn-Schunck optical flow.	37
Figure 4.5	The average pixel shift in the flow on area of singular BOS images processed with Horn-Schunck optical flow plotted against the flow off pixel shift for the same image for each background type at each b/L value. Larger pixel shifts indicate more sensitivity and ability to visualize the plume.	39
Figure 4.6	The average pixel shift for singular BOS images processed with Horn-Schunck optical flow with the flow off pixel shift subtracted at each b/L , where negative values for the projected background are marked on the x-axis of the plot.	39
Figure 4.7	The average pixel shift in the flow on area of singular BOS images processed with wOFA plotted against the flow off pixel shift for the same image for each background type at each b/L value.	40
Figure 4.8	The average pixel shift for singular BOS images processed with wOFA with the flow off pixel shift subtracted at each b/L	40
Figure 4.9	The average pixel shift for singular BOS images processed with Horn-Schunck optical flow compared to the same images processed with wOFA, both with the flow off pixel shift subtracted at each b/L value, where negative values for the projected background are marked on the x-axis of the plot.	41

Figure 4.10 Comparison of a BOS image taken with a b/L of 0.3 using the laser speckle background processed using (a) Horn-Schunck optical flow, and (b) wOFA	41
Figure 4.11 Averaged BOS images processed using Horn-Schunck optical flow for each combination of background and b/L distance, with $Re = 1985$	43
Figure 4.12 average pixel shifts for the flow on portion of fifty BOS images processed using Horn-Schunck optical flow plotted against the average pixel shift for the flow off portion of those images, for each background type and b/L combination.	44
Figure 4.13 average pixel shifts for the flow on portion of fifty BOS images processed using Horn-Schunck optical flow with the average pixel shift for the flow off portion of those images subtracted, for each background type and b/L combination, where negative values for the projected background are ignored.	44
Figure 4.14 Full plume edge detection applied to BOS images processed using wOFA.	45
Figure 4.15 The average pixel shift in the flow on area of singular BOS images processed with Horn-Schunck optical flow plotted against the linear fit for the same data at each b/L value. Steeper slopes indicate more sensitivity and ability to visualize the plume.	47
Figure 4.16 The average pixel shift in the flow on area of singular BOS images processed with wOFA plotted against the linear fit for the same data at each b/L value. Steeper slopes indicate more sensitivity and ability to visualize the plume.	47
Figure 4.17 The average pixel shifts for the flow on portion of fifty BOS images processed using Horn-Schunck optical flow plotted against the linear fit for the same data, for each background type and b/L combination. Steeper slopes indicate more sensitivity and ability to visualize the plume.	48

LIST OF ABBREVIATIONS

r_c	distance from the center of calibration lens
R	radius of calibration lens
f	focal length of lens
ϵ	angle of refraction
ϵ_R	maximum angle of refraction in schlieren calibration lens
n	refractive index
d_e	length of refractive disturbance in a shadowgraph image
d'_e	length of the projection of a refractive disturbance in a shadowgraph image
L	distance from camera to background in BOS and shadowgraphy setups
b	distance from refractive disturbance to background in BOS and shadowgraphy setups
t	distance from camera to refractive disturbance in BOS and shadowgraphy setups
BOS	background oriented schlieren
e	pixel shift in a BOS image
θ	angle from center line of the camera lens
D	fractal dimension
N_r	number of boxes filled when box counting
r	box length when box counting
Re	Reynolds number
Q	volumetric flow rate
ν	kinematic viscosity
d	pipe exit diameter
σ	standard deviation
σ_B	average uncertainty in linear fit used to find fractal dimension of each image
σ_c	smoothing parameter for Canny edge detection
T	threshold for weak edges for Canny edge detection

\bar{u}	local average pixel velocity in the horizontal (x) direction for optical flow
\bar{v}	local average pixel velocity in the vertical (y) direction for optical flow
i	iteration number
E_x	partial derivative of pixel intensity with respect to x (horizontal displacement)
E_y	partial derivative of pixel intensity with respect to y (vertical displacement)
E_t	partial derivative of pixel intensity with respect to t (time)
α	smoothing parameter for optical flow

This thesis is accepted on behalf of the faculty of the Institute by the following committee:

Michael Hargather

Academic and Research Advisor

Austin Mier

Kip Carrico

I release this document to the New Mexico Institute of Mining and Technology.

Maria N. D'Orazio

–, 2025

CHAPTER 1

INTRODUCTION

1.1 Research Motivation

Air leakage out of buildings contributes to reduced building efficiency and durability, and can cause both discomfort and health issues for building occupants [1]. The current method for determining building efficiency is a blower door, which returns an overall building efficiency but cannot locate leaks. Therefore, an efficient method for locating building leaks to be sealed is of interest [2]. Due to internal temperature controls, a building leak will be at a different temperature than the outside air, this difference in temperature causes a density gradient that can be identified using refractive imaging techniques. The motivation of this research is to develop these imaging methods to visualize plumes representing building air leakage.

Schlieren is an imaging technique that visualizes refractive index gradients and can be performed in several ways. Lens-type schlieren systems function by creating a test section with parallel light that is bent by refractive disturbances. Background oriented schlieren (BOS) is another method of schlieren imaging that requires only a camera and a random background to visualize refractive disturbances against [3]. A lens-type schlieren system returns higher quality results, however BOS is useful for the application of building leak detection because it is non-intrusive and can be performed with minimal equipment. An ideal BOS system has significant distance between the event, background, and camera, however in the case of building leakage, the background will be very close to the event decreasing the sensitivity of the BOS system greatly.

Air escapes from buildings through small holes and cracks creating a plume of air at a different temperature than the ambient air outside. A plume with a different temperature, and thus different refractive index, than the ambient air can be easily recreated in a laboratory setting to determine effective methods of plume detection and identification for field applications. Here, the ability to detect plumes and determine their characteristics in schlieren images is explored, as well as the sensitivity limits of BOS in the context of building leakage detection.

1.2 Refractive Imaging Techniques

Refractive imaging allows for the visualization of refractive index fields which can be related back to densities. Here, schlieren, shadowgraph, and background oriented schlieren (BOS) are explained in the context of refractive imaging.

1.2.1 Schlieren

Schlieren imaging is a method of visualizing the first spatial derivative of refractive index [3]. A typical lens-type schlieren system consists of a point like light source one focal length away from a collimating lens that creates parallel light through a test section. A light ray in the test section is then bent by any refractive disturbances present and collected by a second collimating lens that focuses the light back down to a focal point. At the focal point a knife edge is placed to cutoff any light that has been bent by refractive disturbances in the test section. The light then enters a camera and is imaged. A lens-type schlieren system is schematically illustrated in Figure 1.1.

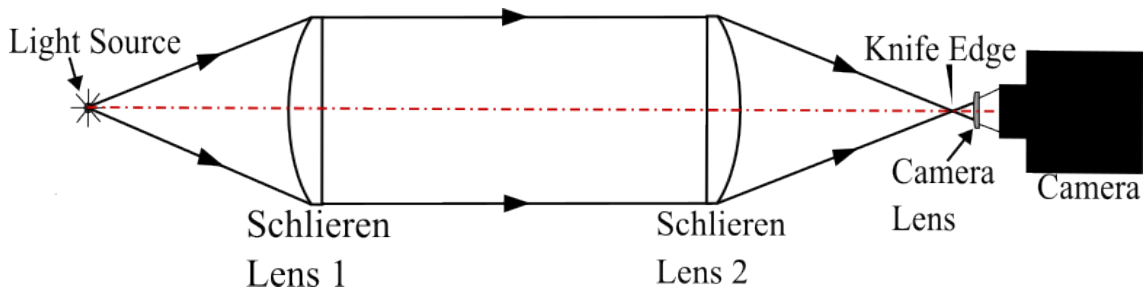


Figure 1.1: Schematic of a lens-type schlieren system

When light is bent inside the test section it is no longer parallel and does not focus to the same place as the rest of the light. So, bent light will either appear darker in the schlieren image due to being blocked by the knife edge, or brighter because light has been bent away from the knife edge and more light is collected by the camera sensor in this area. The knife edge in a schlieren system can be set up in several orientations, and will change the schlieren image accordingly. A vertical knife edge will block light in the horizontal (or x) direction, causing dark to light variation from left to right in the image. A horizontal knife edge will block light in the vertical (or y) direction causing light to dark variation from top to bottom in the image. A circular, or pinhole cutoff can also be used to cut off light in all orientations so all changes in refractive index appear darker than the background intensity. Changing the amount of cutoff will adjust the range of intensities available in the schlieren system, and removing the knife edge from the system completely will result in shadowgraphy [3].

Schlieren can be used for imaging a wide range of flows from weak plumes to strong shocks [4, 5], and it is possible to extract quantitative density field data from schlieren images [6]. To accomplish this, a weak lens with a long focal length (f) is placed inside the test section of the schlieren system. Different points in the lens will be bent at different angles depending on the distance from the center of the lens (r_c). This can be used to relate pixel intensities to angle of refraction (ϵ) [7] as shown in Figure 1.2 using:

$$\frac{r_c}{f} = \tan(\epsilon) \quad (1.1)$$

The angle of refraction is related to refractive index as follows, where x , y and z represent spatial directions and n is the refractive index [3]:

$$\epsilon_x = \frac{1}{n} \int \frac{\delta n}{\delta x} \delta z, \quad \epsilon_y = \frac{1}{n} \int \frac{\delta n}{\delta y} \delta z \quad (1.2)$$

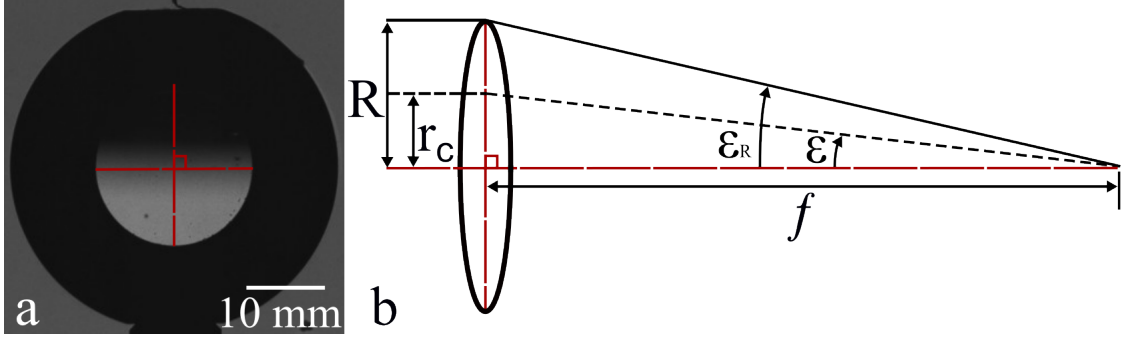


Figure 1.2: (a) An image of a calibration lens in a lens-type schlieren setup compared to (b) an illustration of parallel light passing through a calibration lens with focal length f , where R is the radius of the lens and r_c is the distance from the center of the lens for a given point. ϵ_R represents the maximum refraction angle at the edge of the lens, and ϵ represents the angle of refraction for radius r_c in the calibration lens.

1.2.2 Shadowgraphy

Shadowgraphy is an optical technique that captures the second spatial derivative (Laplacian) of a refractive index field by imaging the shadow that a refractive disturbance casts. Shadowgraphy can be conducted in multiple ways, the simplest of which is direct shadowgraphy shown in Figure 1.3, where light is projected through an event, onto a background. This method of shadowgraphy only requires a light source and a background suitable for imaging. Any flat uniform

background that will suitably reflect light can be used in a direct shadowgraphy system, though often plain white backgrounds or retro-reflective screens are used [8]. Focused shadowgraphy can be performed in a lens-type schlieren system by removing the knife edge and placing a background or camera behind the focal point [3].

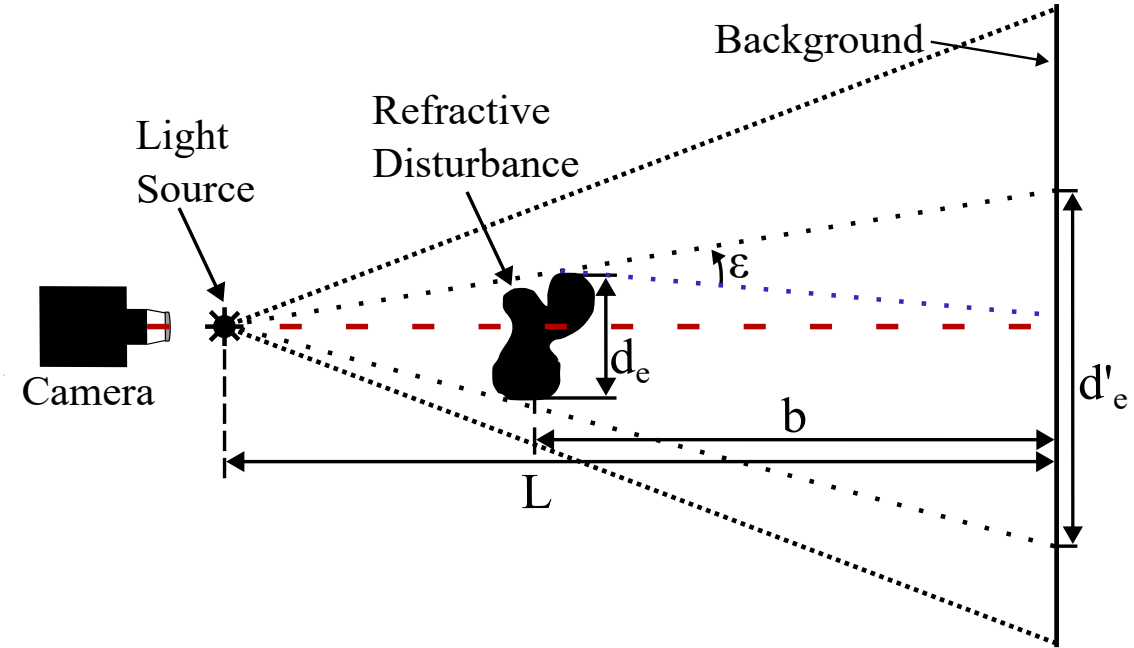


Figure 1.3: Schematic of a direct shadowgraphy system, where the background is a distance L from the camera and a distance b from the refractive disturbance, and ϵ represents the angle of refraction caused by the disturbance. d_e represents the actual length of the disturbance, and d'_e represents the length of the disturbance's projection.

It is important to note that while a schlieren system images an actual refractive disturbance, shadowgraphy images a disturbance's shadow. This means that while schlieren images depict a gradient relating directly to angle of refraction, a shadowgram shows ray displacements resulting from the deflection. Additionally, it is important to remember that the size of a shadowgram is scaled relative to the distance b , between the disturbance and the background, and if additional optics are added to the system, the distortions they cause may need to be accounted for. Ultimately, schlieren images are more sensitive and are capable of returning more quantitative data, but shadowgraphy systems are more easily set up and therefore applicable to a wider range of experiments [8].

1.2.3 Background Oriented Schlieren

Background oriented schlieren (BOS) is a technique where refractive disturbances are imaged against a background with intensity variation in order to determine angle of refraction using image correlation techniques. A conventional BOS system consists of only a camera and a background as illustrated in Figure 1.4. Increasing the distance b between the background and the refractive disturbance will generally result in a more sensitive BOS system. A BOS system's sensitivity is largely defined by the ratio of the distances t between the camera and the refractive disturbance, L between the camera and the background and b between the background and the refractive disturbance. The ratio t/L or b/L can be used to describe the background placement in a BOS system and the two quantities sum to one:

$$\frac{t}{L} + \frac{b}{L} = 1 \quad (1.3)$$

Ideally the ratio of the distance b and the distance L is greater than 0.25. For proper BOS imaging, both the refractive disturbance and the background should be relatively in focus, and this becomes hard to achieve for b/L greater than about 0.5 [9]. It has also been shown that increased camera lens focal length, and a smaller lens aperture can increase the sensitivity of BOS systems [10–12].

The presence of a refractive disturbance between the camera and the BOS background causes an apparent pixel shift in the background from the camera's perspective. By measuring this pixel shift it is possible to calculate the refractive angle of a disturbance. If e is the measured pixel shift, b is the distance from the refractive disturbance to the background, ϵ is the angle of refraction, and θ is the angle from the center line of the camera as shown in Figure 1.4, the following formula can be used to determine angle of refraction [9]:

$$e = b * [\tan(\theta) - \tan(\theta - \epsilon)] \quad (1.4)$$

If one uses the small angle approximation for tangent, $\tan(\theta) \approx \theta$, and rearranges to solve for ϵ the above equation becomes:

$$\epsilon = \frac{e}{b} \quad (1.5)$$

A BOS background can be any surface with sufficient intensity variation to allow for the visualization of refractive disturbances. Often a random dot background is used [10], but one can use a color or gray scale gradient [9], laser speckle [13], or even the surface of a hillside [14]. The versatility of BOS backgrounds makes it ideal for experiments that cannot be conducted in a controlled laboratory environment. Recently BOS has been applied to the visualization of convective indoor flows, and ventilation flows inside of buildings [15, 16], as well as air leakage out of buildings [1].

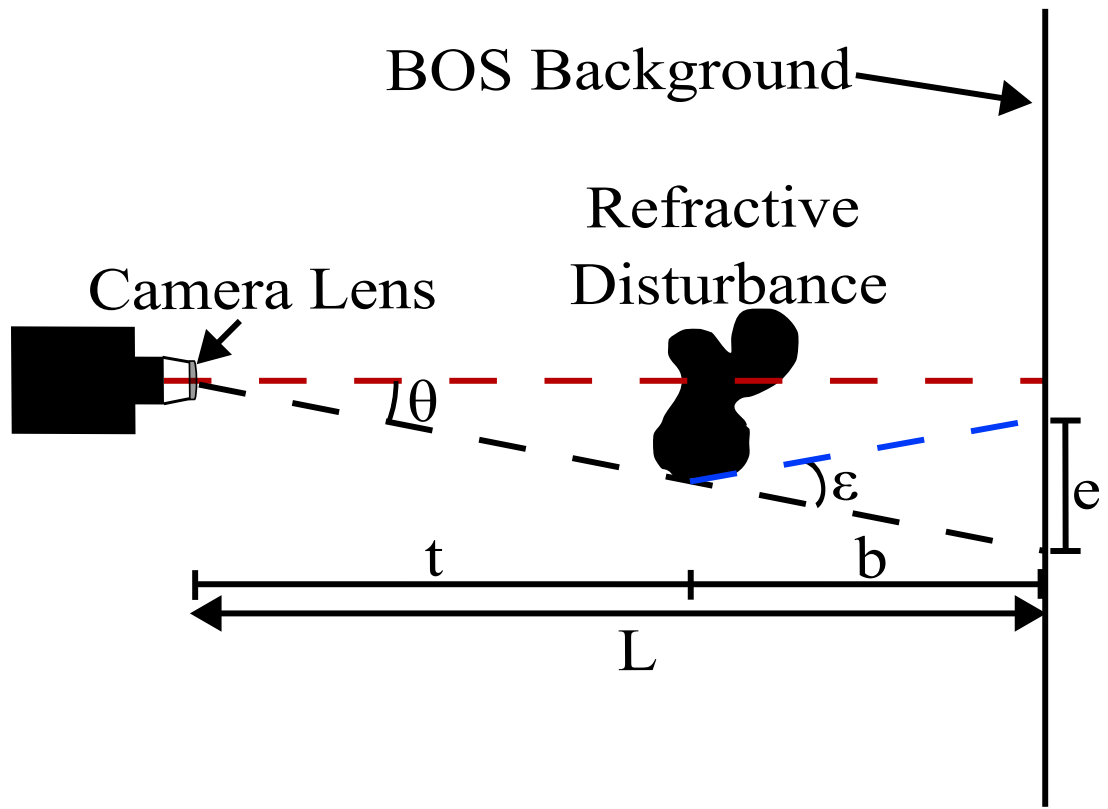


Figure 1.4: General BOS setup where L is the distance between the background and the camera, t is the distance from the camera to the refractive disturbance, b is the distance from the refractive disturbance to the background, e is the measured pixel shift, θ is the angle measured from the center line of the camera, and ϵ is the angle of refraction.

The benefits of non-traditional BOS backgrounds have been explored in recent research. Boudreaux et al. (2022) experimented with using the texture of a building’s surface as the background for BOS images, rather than attempting to insert a background [1]. Lyu et al. (2024) projected a background onto a screen from behind so that the background could be manipulated in real time depending on the needs of their setup [17]. Weisberger and Bathel (2022) used a beam splitter to project their BOS background simultaneously through their event and at a reference camera so that they would have background images for each individual frame, allowing for real time BOS processing with perfectly accurate background images [18]. Raffel et al. (2024) conducted BOS experiments with a laser speckle background projected through a helium plume. Projecting this laser light through the refractive event resulted in a “forward BOS” image alongside a standard BOS image. This “forward BOS” image is a shadowgram cast by the laser light. So, when processed, the images showed both a standard BOS pixel shift, and a shadowgram of the event in different areas of the same image [13]. The wide array of BOS background possibilities allows for BOS to be applicable in many different scenarios.

BOS systems can achieve relatively high sensitivity [19], be used to gather quantitative data, and require minimal equipment. BOS’s versatility and accuracy make it an ideal candidate for building leakage detection.

1.3 Fractal Behavior and Box Counting

Fractals are complex shapes that exhibit self-similar or self-affine behavior, meaning parts of a fractal object relate to the whole in some way [20]. Examples of fractal behavior can be seen throughout nature including the surface/edge patterns of mountains, clouds, or leaves [21]. In 1975, Mandelbrot coined the term fractal dimension to quantify fractal behavior, and this value corresponds closely to observable roughness of an object [22].

Box counting is a simple and common method of determining fractal dimension that divides an image into squares or “boxes” of decreasing size, and counts the number of non-zero pixels in each box. For each box length (r), the number of boxes containing non-zero pixels (N_r) are counted and plotted on a logarithmic scale, the slope of the line obtained from plotting $\log(N_r)$ against $\log(\frac{1}{r})$ returns an overall fractal dimension for the image. The below equation is used to determine fractal dimension (D) at a specific r value [23]:

$$D = \frac{\log(N_r)}{\log(\frac{1}{r})} \quad (1.6)$$

The idea that turbulence is an example of fractal behavior was first suggested by Mandelbrot in 1975. When observing turbulent flows it is easily observable

that eddies swirling off of each other exhibit the self-affine behavior characteristic of fractals [24]. Since then, many attempts have been made at characterizing the fractal behavior of turbulence [25]. Prasad and Sreenivasan attempted to obtain a value for the fractal dimension of turbulence by imaging the scalar surface of two dimensional (2D) water jets in the axial direction. They accomplished this by using a florescent dye to distinguish the jet from its surroundings and illuminating it with laser induced florescence (LIF) [20, 26]. Lane-Serff conducted very similar experiments soon after, with jets in the transitional and turbulent regimes and determined a lower fractal dimension [27]. Sykes and Gabruk performed fractal analysis on large-eddy simulations (LES) of plume dispersion, resulting in a fractal dimension in between the values that Prasad and Lane-Serff obtained [28]. Catrakis utilized LIF to visualize turbulent jets as well, but observed the jets radially rather than axially, their work suggested that the fractal dimension of turbulence was scale dependent and therefore did not report a specific value for turbulent fractal dimension. Each of these experiments used box counting on edges found in experimental images as a means of fractal analysis, and their reported fractal dimensions are listed in Table 1.1.

Table 1.1: Previously published values for fractal dimension of turbulent plume edges.

Fractal dimension (D)	Re Range	Citation	Technique
1.23	800-1800	Lane-Serff [27]	Axial LIF imaging of water jet
1.36	4000	Prasad and Sreenivasan [26]	Axial LIF imaging of water jet
1.30 - 1.35	Infinite Re Simulation	Sykes and Gabruk [28]	Simulation of turbulent boundary layer
Scale-dependent D	4500 - 18000	Catrakis [29]	Radial LIF imaging of water jet

1.4 Image Processing

A raw experimental image provides an initial amount of information on the event that it captures, it is possible to extract further quantitative data from images by applying certain processing methods. Image processing encompasses a wide range of techniques that are used to extract quantitative data from images.

1.4.1 Optical Flow

In image processing, optical flow is the apparent velocity of objects moving in an image based on shifts in pixel intensity. It can be used to determine flow behavior from successive images of the flow. Optical flow is often applied to BOS image processing because it allows for the calculation of the apparent pixel displacement from one image to another [30]. A common optical flow method is the Horn-Schunck method which assumes a flat surface with uniform illumination is imaged, and that intensity variation is smooth everywhere. The Horn-Schunck method uses an iterative approach to solve for velocity vectors in the x and y direction, u and v respectively, at each point in an image using [31]:

$$u_{i+1} = \bar{u}_i - E_x \frac{E_x \bar{u}_i + E_y \bar{v}_i + E_t}{\alpha^2 + E_x^2 + E_y^2} \quad (1.7)$$

$$v_{i+1} = \bar{v}_i - E_y \frac{E_x \bar{u}_i + E_y \bar{v}_i + E_t}{\alpha^2 + E_x^2 + E_y^2} \quad (1.8)$$

the variable α is a smoothing parameter chosen by the user to account for the expected noise in an image. \bar{u} and \bar{v} represent local average velocities in the x and y directions respectively, u_{i+1} , and v_{i+1} represent new iterative guesses for the local average velocity at a point. E_x , E_y , and E_t represent the partial derivatives of image pixel intensity with respect to x , y , and t respectively where x and y are spatial directions and t represents time.

The Horn-Schunck method is a gradient based approach to optical flow, it is also possible to take a wavelet based approach. In 2021, Schmidt and Woike developed an optical flow algorithm using wavelet-based optical flow analysis (wOFA), which solves for displacements in the wavelet domain rather than the spatial domain, and has been shown to outperform gradient based approaches for some applications [32]. The algorithm published by Schmidt and Woike solves for displacements in BOS images, using their wavelet based approach, and outputs processed BOS images.

1.4.2 Edge Detection Techniques

Edge detection is a category of image processing techniques that are used to isolate objects of interest in images. Here, an edge is defined as the outside limit of an object in an image and is characterized by an abrupt change in pixel intensity. The most basic method of edge detection is thresholding, in which all pixels above or below a certain intensity are ignored. This method is useful only if the object of interest has significant contrast from the image background in all areas. For example, Sreenivasan (1991) and Lopez (2017) were able to use thresholding

to find the edges of jets in their experiments because they used dyes to distinguish their jets from the ambient environment [20, 25]. In many cases edges are not necessarily so distinct from the background of an image, for these cases edge detection techniques that determine the gradient of pixel intensity at each point are more widely applicable. For example, Prasad (1989) computed the Laplacian of pixel intensity to locate edges in turbulent jet images [26], and Lazzaro developed an edge detection approach that combined iterative thresholding and pixel intensity gradients to detect edges in schlieren images of turbulence [33, 34].

One of the more widely used methods of edge detection is Canny edge detection, a robust method involving four main steps [35]. First the image is lightly smoothed with a Gaussian filter, the strength of which is determined by the parameter σ_c . Next, intensity gradients and their directions are determined for every pixel in the image. Then, pixels with gradients greater than their neighbors in the same direction are marked as edges. Lastly a threshold, T , is applied to eliminate weak edges [36]. This method is very effective at determining edges of any strength, but it is important to remember that the smoothing step can cause a loss of resolution for fine details.

Normally, images exist in the spatial domain, meaning that each pixel corresponds to a point in space and contains an intensity value to reflect that spatial point. The previously described techniques are all applied in the spatial domain. Using a Fourier transform, an image can be converted from the spatial domain into the frequency domain, where an image is represented as a series of frequencies that are related to spatial rates of change in the image's pixel intensities. In the frequency domain, a sharp edge with high contrast from the background would exist as a high frequency value, while a blurry edge or one poorly contrasted from the background would exist as a low frequency value. This makes the frequency domain useful for edge detection, because sharp edges can be quickly and easily distinguished from low contrast areas of an image. In order to accomplish this, high and low pass filters are used. A high-pass filter attenuates low frequencies and leaves high frequencies unchanged, this results in sharpened edges but reduced contrast. A low-pass filter does the opposite, it attenuates high frequencies and leaves low frequencies unchanged, so it blurs the details of an image. Both of these techniques can be useful, but high-pass filters are often used for edge detection. Once image processing has been performed in the frequency domain, an inverse Fourier transform can be performed to convert the image back to the spatial domain for viewing [37]. Many programs such as MATLAB have built in functions to convert between the spatial and frequency domains [38, 39]. Figure 1.5 shows the difference between an image in the spatial domain and an image in the frequency domain.

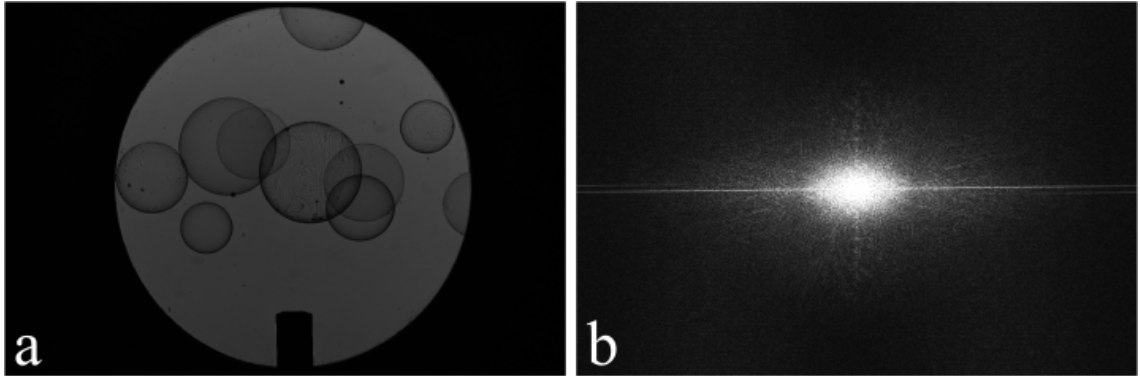


Figure 1.5: The same lens-type schlieren image of bubbles in the (a) spatial domain and (b) frequency domain shifted so that the lowest frequencies are in the center of the image

1.5 Research Objectives

The research here is a fundamental examination of methods to characterize plumes visualized with refractive methods, which will provide a basis from which to develop technology to visualize air leakage in buildings. The two main goals of this work are to:

- Detect edges in schlieren images of plumes and use them to determine the flow regime and approximate Reynolds number of the flow.
- Find limits of detection for BOS with a background projected through an event and compare to BOS with a physical background to determine at what point the resolution needed for quantitative analysis is lost, and determine what method of optical flow is most effective for the application of building leakage.
- Develop recommendations for implementing a BOS method for detecting building leaks and their characteristics.

CHAPTER 2

EXPERIMENTAL METHODS

A schlieren system was set up to image helium plumes in air transitioning from laminar to turbulent flow regimes over twelve Reynolds numbers. A BOS system was set up with three different types of BOS background to image turbulent helium plumes in air at six different b/L distances varying from 0.035 to 0.5.

2.1 Lens-type Schlieren and Shadowgraphy

Schlieren and shadowgraph images were recorded using a lens-type system as illustrated in Figures 2.1 and 2.2. A white SugarCUBE LED with a 5 mm diameter liquid light guide was used as the light source for this setup. Schlieren lenses with 700 mm focal lengths and 127 mm diameters were used to collimate and focus the light. For imaging, an 80-200 mm variable focal length lens was attached to a Photron FASTCAM Mini high speed camera operating at 3000 frames per second with a shutter speed of $1.1 \mu\text{s}$, and the aperture set to $f/2.8$. A volumetric flow meter calibrated for helium flow between 0 and 500 L/min was used to measure flow rates in the system. Flow rates were controlled manually using the helium tank valve and monitored using the flow meter.

Five cutoff orientations were utilized for imaging: vertical cutoff, horizontal cutoff, circular cutoff, and shadowgraphy (no cutoff) in and out of focus, these cutoffs are represented in Figure 2.3. For each cutoff orientation, 12 Reynolds numbers spanning laminar, transitional, and turbulent flow regimes were imaged: 200, 400, 600, 775, 800, 835, 895, 990, 1190, 1985, 2580, and 2980. Flows for each of these Reynolds numbers are depicted in Figure 2.4, representative images for the flow regimes are shown in Figure 2.5, and the corresponding jet exit velocities for each Reynolds number are listed in Table 2.1. At each cutoff and Reynolds number combination 1000 grayscale images were recorded with a resolution of 1024 by 1024 pixels, which corresponded to a pixel resolution of 7.53 pixels/mm.

Reynolds number (Re) was calculated for each test from the measured volumetric flow rate (Q) and the known pipe diameter (d)

$$Re = \frac{4Q}{\pi v d} \quad (2.1)$$

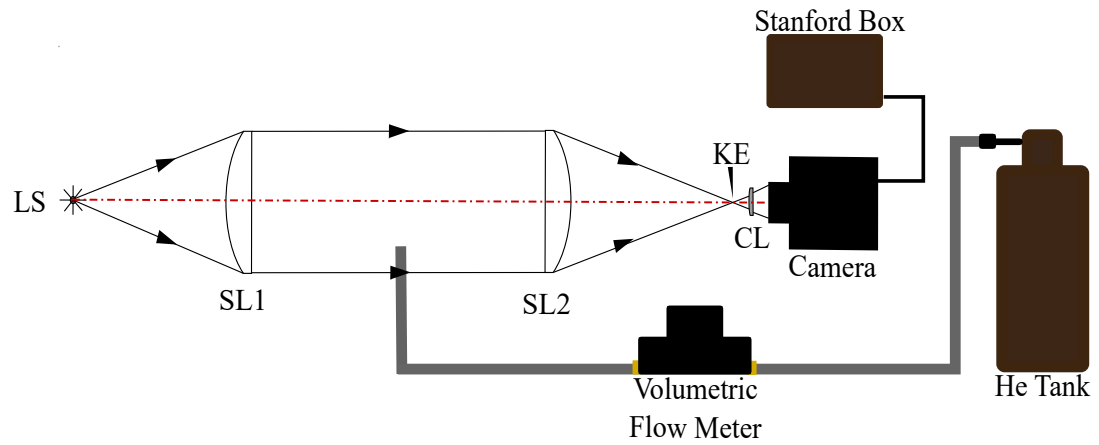


Figure 2.1: Schematic of schlieren setup used for imaging helium plumes where LS represents the light source, SL1 and SL2 are the collimating and refocusing schlieren lenses, respectively, KE represents the knife edge, and CL represents the camera lens. The shadowgraphy system is identical to the schlieren system with the knife edge removed.

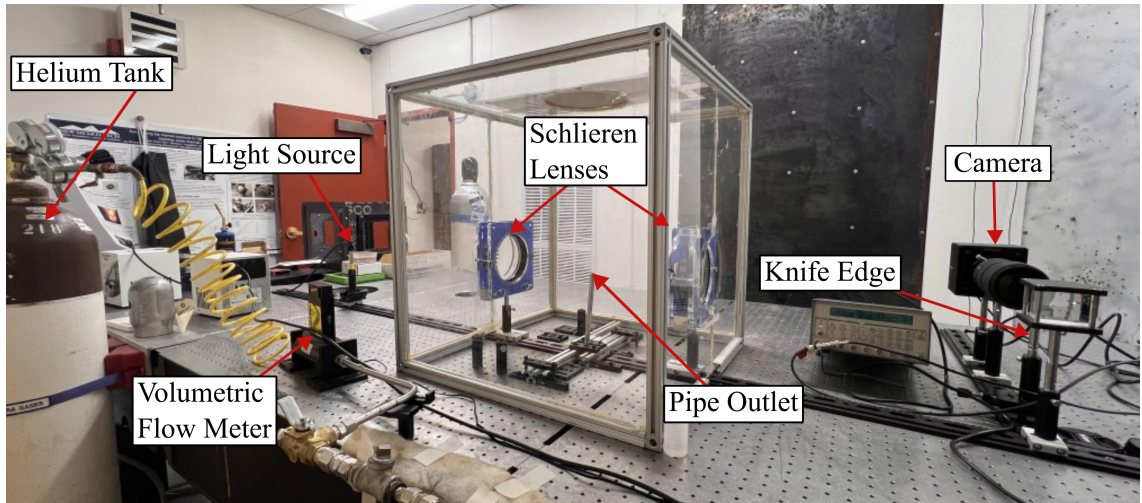


Figure 2.2: Image of the experimental setup for schlieren and shadowgraph images of helium plumes.

Table 2.1: Jet exit velocity values corresponding to individual Reynolds numbers

Reynolds Number	Velocity (m/s)
200	2.76
400	5.53
600	8.29
775	10.75
800	11.06
835	11.60
895	12.44
990	13.82
1190	16.58
1985	27.64
2580	35.93
2980	41.46

The pipe exit diameter was 9 mm and the kinematic viscosity (ν) was 0.000122 m²/s based on the thermodynamic property relationships published by Peterson [40] for atmospheric pressure and the measured temperature. The plumes were analyzed from the jet exit to a distance of 10.5 jet diameters downstream.

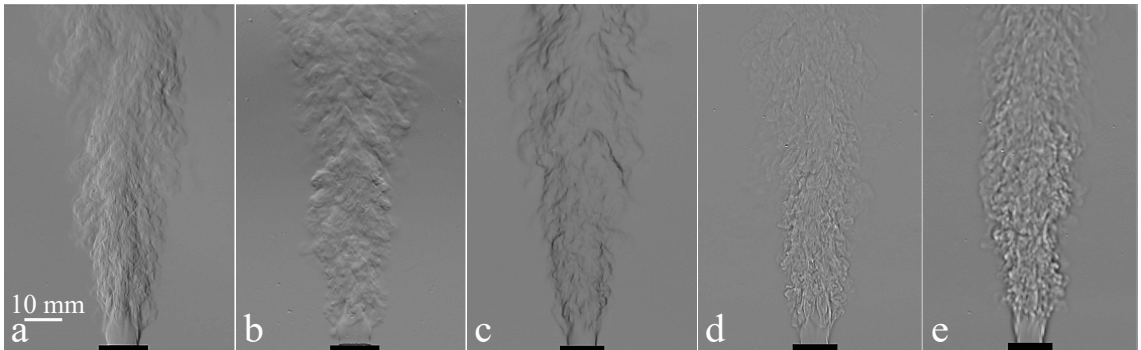


Figure 2.3: Examples of each type of cut off for a helium plume with a Reynolds number of 1985: (a) vertical cutoff, (b) horizontal cutoff, (c) circular cutoff, (d) focused shadowgraphy, (e) de-focused shadowgraphy.

A singular high resolution (4024 pixels by 6048 pixels) image with a pixel resolution of 27.67 pixels/mm was taken at Reynolds numbers of 895 (transitional), 1985 (turbulent) and 2185 (turbulent) for each cutoff type using a Nikon D780 camera. These images were used to determine if image resolution had a signifi-

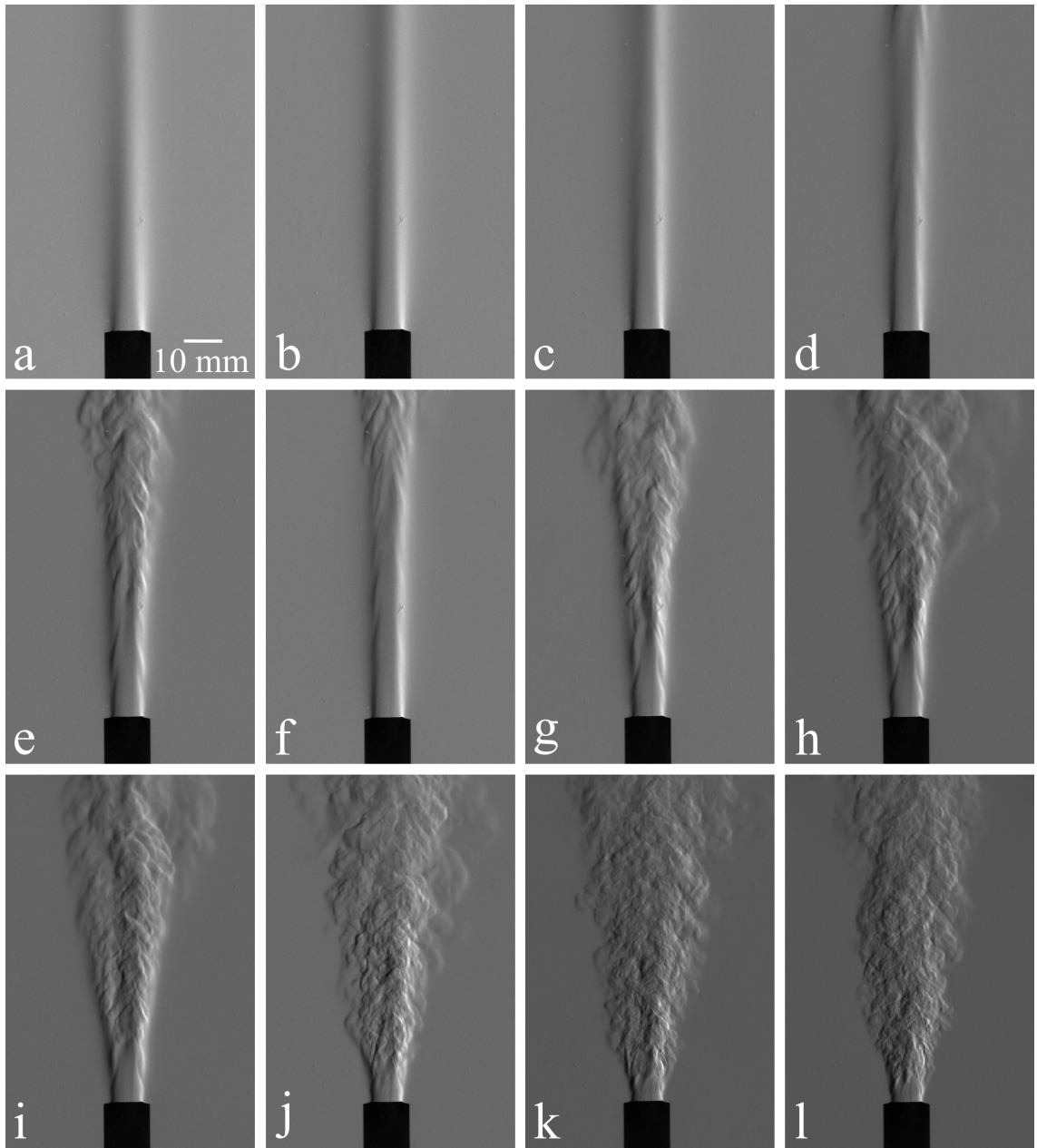


Figure 2.4: Vertical cutoff schlieren images representing each Reynolds number imaged: (a) 200, (b) 400, (c) 600, (d) 775, (e) 800, (f) 835, (g) 895, (h) 990, (i) 1190, (j) 1985, (k) 2580, and (l) 2980.

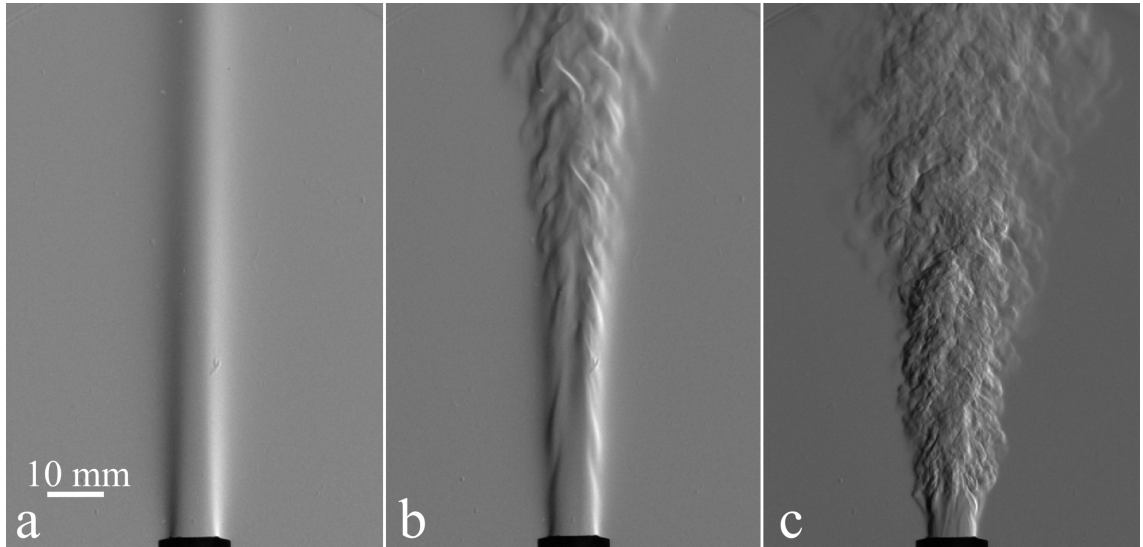


Figure 2.5: Helium plumes with a vertical cutoff representing each flow regime at Reynolds numbers of (a) 400 (laminar), (b) 800 (transitional), and (c) 2980 (turbulent).

cant impact on the measured fractal dimension of the plumes. The shutter speed for the camera in these images was $125 \mu\text{s}$, and the same schlieren system was used for imaging.

2.2 Background Oriented Schlieren

Helium plumes were imaged against three different types of BOS backgrounds: a printed background, a projected background, and a laser speckle background, which are depicted in Figure 2.6. The printed background consisted of a random dot background printed onto a 1.02 by 1.52 meter foam core board. The projected background utilized the same random dot background printed on a transparency sheet that was projected by an Apollo Horizon 2 overhead projector. Laser speckle was created by shining a green laser pointer through a glass dispersion filter. A 7.1 megapixel Blackfly S USB3 camera with an 80-200 mm variable focal length lens, recording at 50 frames per second with an exposure of 15 ms, was used for imaging in the setup as seen in Figures 2.7 and 2.8. Fifty BOS images of plumes with Reynolds numbers of 1985 (corresponding to a jet exit velocity of 27.64 m/s) were taken at b/L distances of 0.035, 0.1, 0.2, 0.3, 0.4, and 0.5 for each background type, where b was varied and t was fixed at 2.108 meters.

A shorter exposure time is more ideal for resolving the turbulent plumes captured here because they are moving so quickly. The outlet Reynolds number of 1985 corresponds to an exit velocity of 27.64 m/s. Because the camera exposure could not be put lower than 15ms due to available light, points in the helium plume were able to travel up to 414.6 mm in the time that it took the camera to capture a single frame. The camera resolution was 2200 by 3208 pixels which corresponds to a field of view of 239.75 by 349.60 mm in the plane of the plume, meaning that it was likely that a single point in the flow was able to travel across the entire imaging frame in the time that it took for the frame to be captured. This is important to note when observing processed BOS images, as it means that the paths that points in the plume traveled are likely being resolved rather than a true instantaneous moment in the flow.

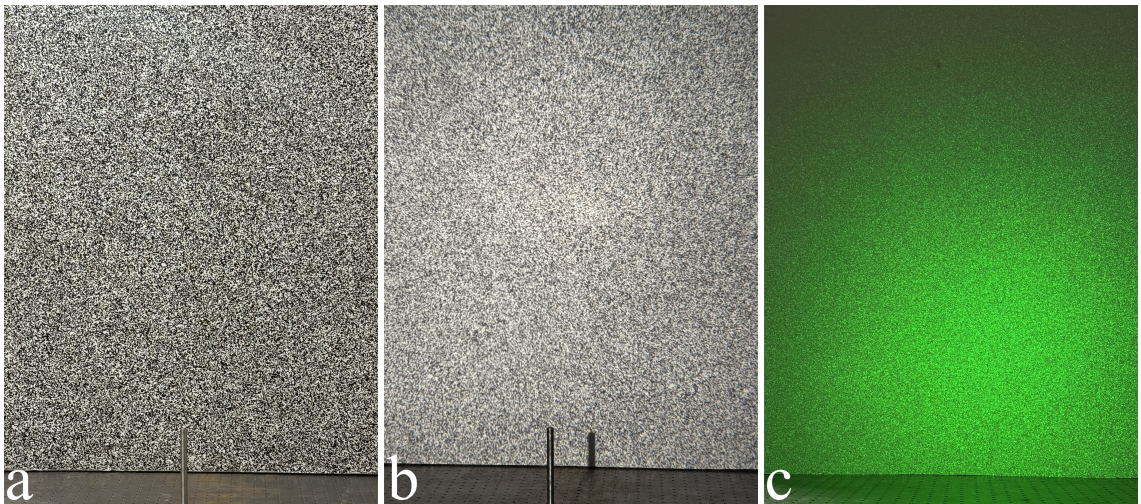


Figure 2.6: Types of BOS backgrounds: (a) printed background, (b) projected background, and (c) laser speckle background.

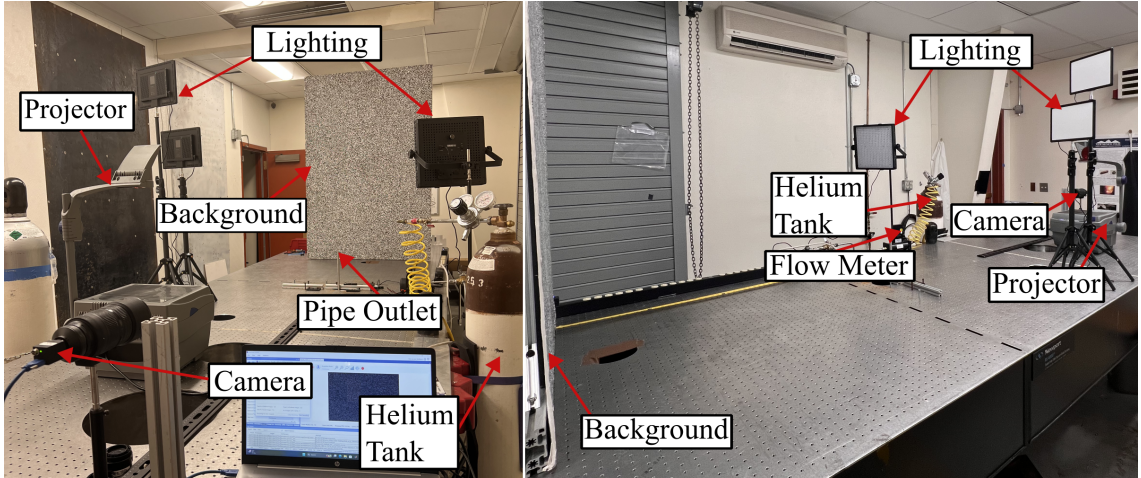


Figure 2.7: Two views of the BOS setup used to image helium plumes.

When imaging against the printed background, LED panels were used to evenly illuminate the background without casting shadows of the event. For both the projected and laser speckle backgrounds, the room lights were turned off and all illumination came from the backgrounds themselves, which were projected on to solid white 1.02 by 1.52 meter foam core boards. For tests with the projected backgrounds and a b/L less than 0.4, the light projecting the background can be seen casting a shadow similar to the "forward BOS" observed by Raffel in 2024 [13], referred to here as a shadowgraph effect, and demonstrated in Figure 2.9. The same phenomenon is seen in BOS images with a laser speckled background and a b/L less than 0.2.

For all BOS images a focal length of 80 mm was used for the camera lens, and the aperture was varied depending on available light, these aperture values are tabulated in Table 2.2. The resolution of BOS images taken with the BlackFly camera was 2200 by 3208 pixels, the pixel to mm calibration was performed for the background at each b/L , these are listed in Table 2.3. In the BOS systems, plumes are imaged from the jet exit to 23.2 diameters downstream from the pipe outlet.

Table 2.2: Lens $f/\#$ used for each BOS experiment

Background Type	$b/L = 0.035$	$b/L = 0.1$	$b/L = 0.2$	$b/L = 0.3$	$b/L = 0.4$	$b/L = 0.5$
Printed	11	11	11	11	11	11
Projected	8	8	8	8	8	8
Laser Speckle	11	11	11	11	8	8

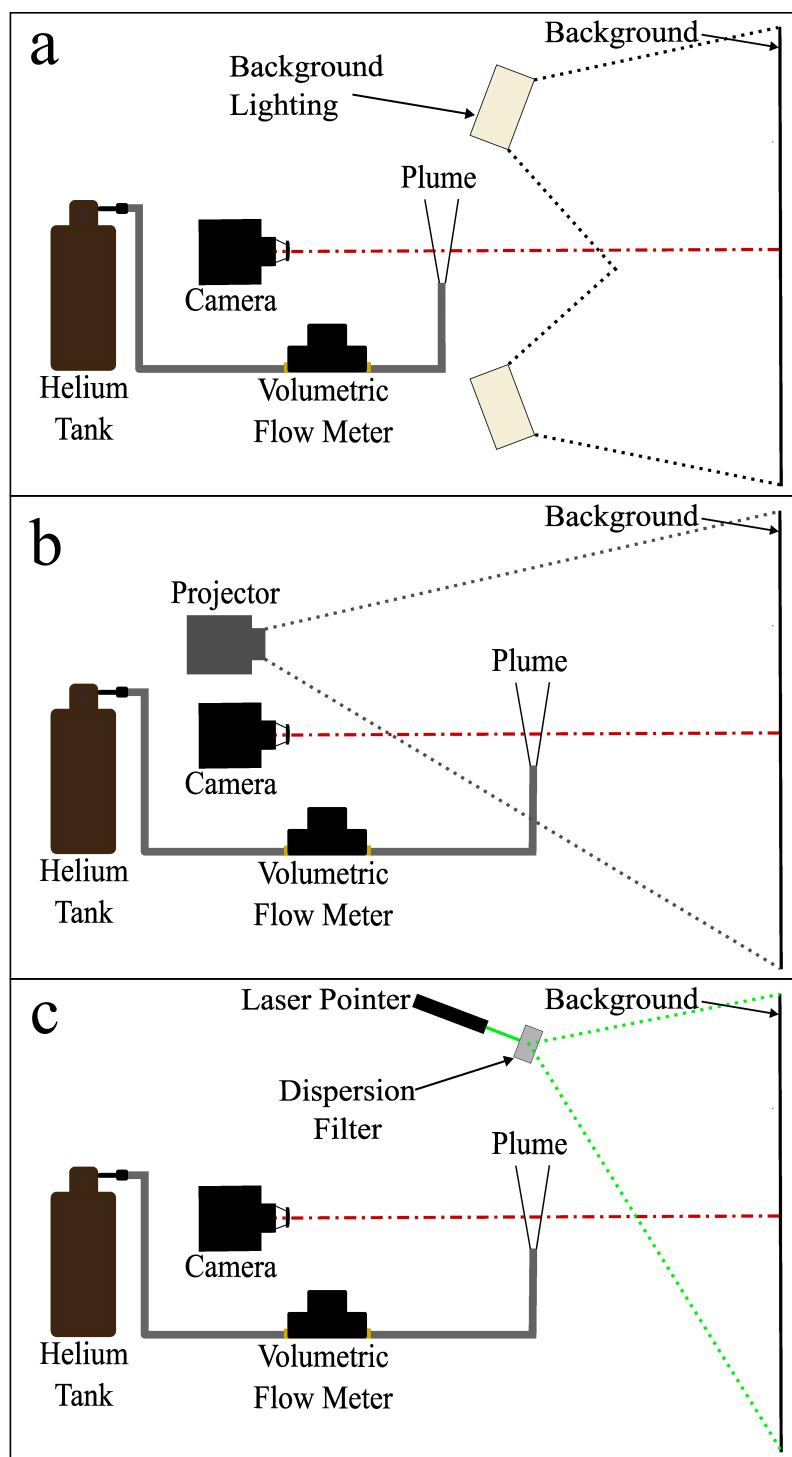


Figure 2.8: Schematic of BOS Setup for imaging helium plumes with (a) the printed background, (b) the projected background, and (c) the laser speckle background.

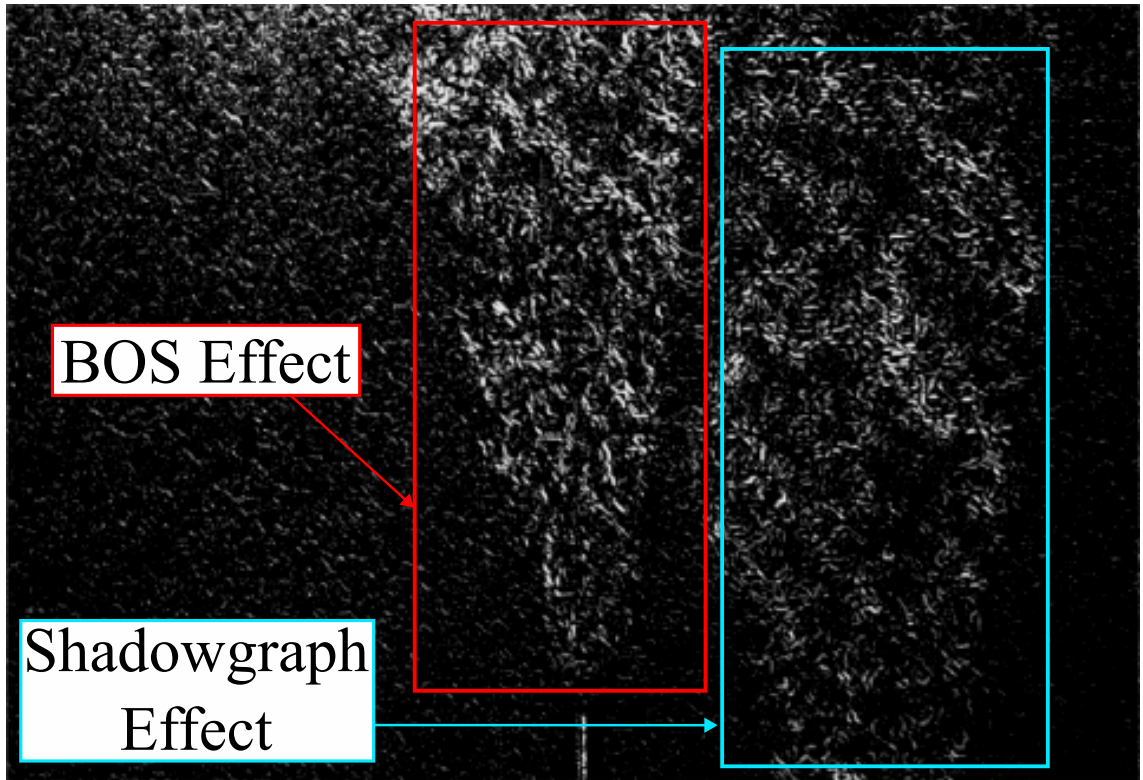


Figure 2.9: Demonstration of the shadowgraph effect caused by the projected background at $b/L = 0.3$. The shadowgraph effect is offset down and to the right because the light was above and to the left of the camera as shown in Figure 2.8b

Table 2.3: Pixel per mm ratio for the background at each b/L distance

	Plume Plane	$b/L = 0.035$	$b/L = 0.1$	$b/L = 0.2$	$b/L = 0.3$	$b/L = 0.4$	$b/L = 0.5$
pix/mm	9.176	8.843	8.239	7.371	6.312	5.348	4.466

2.2.1 BOS Processing Optical Flow Methods

BOS images must be processed in order for the refractive disturbances they capture to be visible. Here, optical flow methods are used to determine pixel shifts in the image. First, the Horn-Schunck method of optical flow, described in equations 1.7 and 1.8, is used to determine pixel shifts in the horizontal and vertical directions of BOS images. Using the Horn-Schunck method, processed BOS images can be created where each pixel intensity value in the image is the magnitude of the pixel shift between a working image and a background image. The overall pixel shift magnitude is found by combining the magnitude of the shift in the horizontal and vertical directions. The difference between a raw BOS image, and one processed using the Horn-Schunck method is demonstrated in Figure 2.10. Ideally a flow off image would be used for the background image in optical flow processing, however for the application of building leakage, it is not possible to take a flow off image, so for all analysis here, an initial flow on image is treated as the background image.

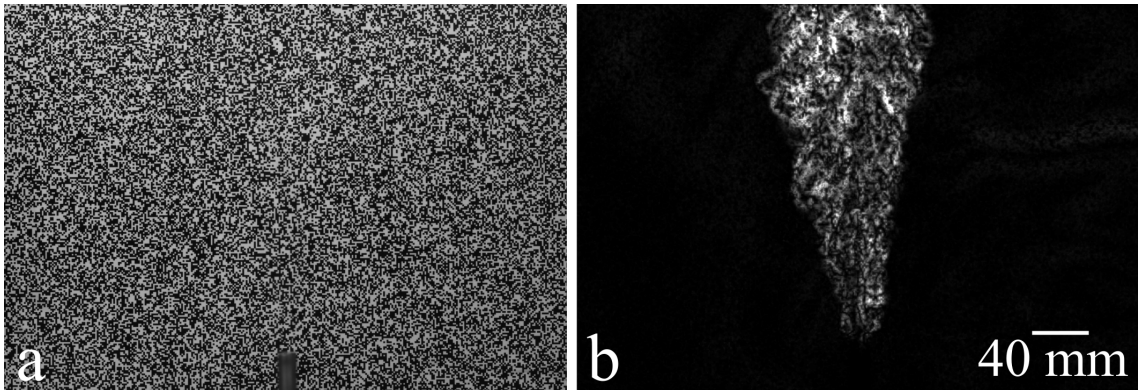


Figure 2.10: (a) Raw BOS image with $b/L = 0.4$ of helium plume with $Re = 1985$ compared to (b) the same image processed through Horn-Schunck optical flow using a flow on background image.

The wavelet based optical flow analysis (wOFA) code developed by Schmidt and Woike [32] is also used for processing here. For the inputs of the wOFA code, an initial flow on image is used as the background image, shift correction is used, and a section from the bottom right corner of the image is selected for shift correction. No mask is used, and the smoothing parameter is left at the default value of 50. Output images are saved as 16 bit displacement magnitude images with an intensity range from 0 to 1. Figure 2.11 shows a raw BOS image compared to one processed using the wOFA code.

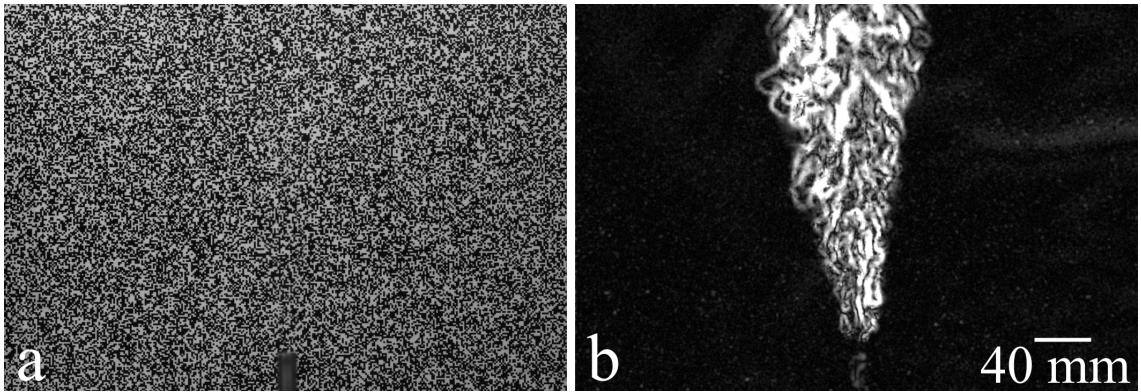


Figure 2.11: (a) Raw BOS image with $b/L = 0.4$ of helium plume with $Re = 1985$ compared to (b) the same image processed through wOFA using a flow on background image.

CHAPTER 3

SCHLIEREN AND SHADOWGRAPHY PLUME DETECTION AND RESULTS

Canny edge detection was applied to helium plumes imaged in the schlieren system, in order to perform fractal analysis on the plumes. This was done in two ways, an edge only edge detection where only the outside edge of the plume was detected, and a full plume edge detection where the outer edges and everything inside of them was detected. Results from each of these edge detection methods for each cutoff type and flow rate tested are presented, as well as the methods for box counting used. Vertical cutoff schlieren was found to yield the best results, and fractal dimension was found to increase with Reynolds number as well as distance from plume outlet.

3.1 Edge Detection Techniques

For each cutoff and flow rate combination in the schlieren setup, 1000 images were taken at a resolution of 1024 by 1024 pixels. Each individual schlieren image was processed to find the fractal dimension at each flow rate through box counting. For effective box counting, a binary image showing the plume's edge is ideal. To achieve this, each image was processed through a MATLAB code to produce a binary image of the plumes' edges. The image processing sequence began with background subtraction, for which a background image was recorded at each cutoff with no disturbance in the test section, i.e., no flow through the pipe. To perform background subtraction, the matrix of pixel intensities for the background image is subtracted from the matrix of pixel intensities for the working experimental image. If desired, the average background intensity can be added back to the image for viewing. The process of background subtraction helps to remove noise present in the background of the image.

Once schlieren and shadowgraph images have been background subtracted the edge detection process can then be performed. First, the image is shifted into the frequency domain using MATLAB's *fft2* function, and shifted so the lowest frequencies are in the center of the image, then a high-pass Gaussian filter is applied. This filter sharpens the edges of the plume and minimizes image noise. MATLAB's edge detection function *edge* with the input *canny* was then applied

to the processed image to isolate the edges of the plume using $\sigma_c = 4$. The threshold value for the Canny *edge* function was varied for each cutoff and flow region combination to obtain the best detection as listed in Table 3.1. A representative image of each of the image processing steps is shown in Figure 3.1.

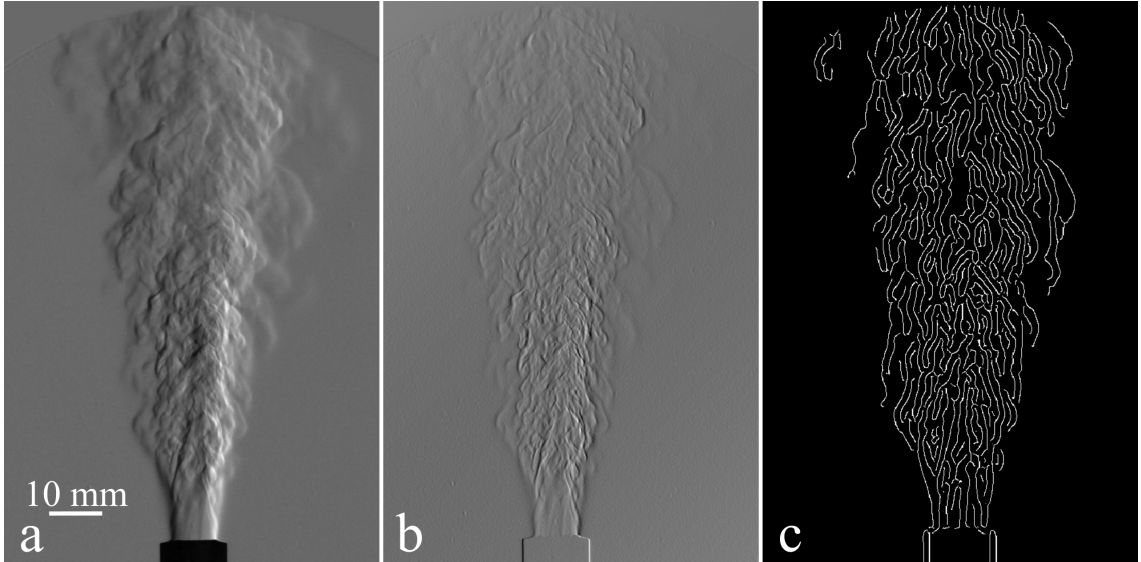


Figure 3.1: Image processing steps demonstrated for a $Re = 1985$ plume with vertical cutoff schlieren imaging: (a) background subtracted original image (b) image after high pass Gaussian filter (c) canny edge detection.

Table 3.1: Threshold (T) values used for the MATLAB *edge* function based on flow region, and cutoff orientation, where SG is shadowgraph

Region	Vertical	Horizontal	Circular	Focused SG	de-focused SG
Laminar	0.1	0.5	0.15	0.3	0.25
Transitional	0.1	0.5	0.15	0.3	0.15
Turbulent	0.1	0.5	0.1	0.1	0.15

Noise was removed from the edge-detected images in two ways: noise outside the plume was removed to create a “full plume edge detection”, and the edges detected inside of the plume were removed to isolate the outer edge of the plume in an “edge only edge detection”. To remove noise outside of the plume, a mask was created around the plume, and multiplied by the processed image to delete all noise outside of the plume. To remove the interior edges, a MATLAB code was written to detect edges that were located between other edges. All edges that had other edges located on both sides were deleted, leaving only the

outer edges of the plume. The difference between the two types of edge detection is shown in Figure 3.2. It should be noted that the full plume edge detection represents a projection of a three dimensional plume rather than a true two dimensional edge as is often used for box counting. The edge only edge detection provides significantly less resolution (length of edge), but provides a more representative 2D slice of the image. The full plume edge detection includes multiple planes of the plume but provides enough resolution for effective box counting.

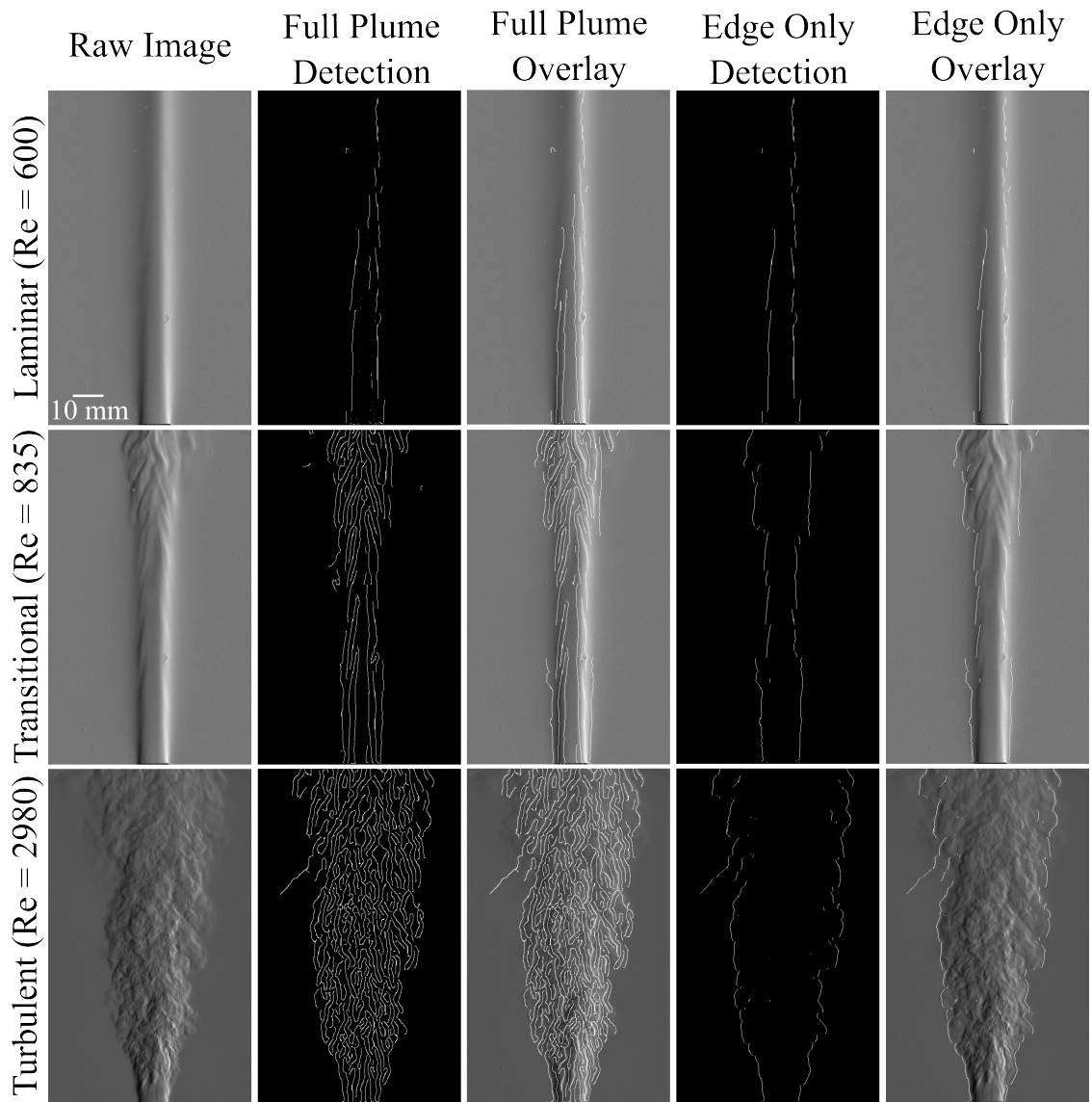


Figure 3.2: The raw images of a laminar, transitional, and turbulent plume imaged with vertical cutoff shown with edge only and full plume edge detection, as well as both edge detection methods overlaid on the raw image of the plume.

3.1.1 Box-counting Methods

Once the edges of the helium plumes have been found for each image, the fractal dimension of the flow can be determined using a box counting algorithm. To determine the fractal dimension of a single image, the image must be subdivided into boxes of decreasing side length r , in which the number of non zero pixels N_r are counted. The local fractal dimension is then determined for each box size, and plotted as shown in Figure 3.3. The overall fractal dimension of the image is determined by calculating the slope of the line that can be fit to the plotted local fractal dimension points, the "Fitted Line" in Figure 3.3. The box counting algorithm used here pads images with zeros to create an image that is 2^n by 2^n pixels before applying box counting so that the image can be properly subdivided into perfect squares down to a side length of one pixel. Due to the padding at different image resolutions, the fractal dimension tends to be more accurate when the original image resolution is a power of 2, i.e., 2^n by 2^n pixels [41]. For each 1000 image set, fractal dimension for a given Reynolds number and cutoff combination was determined by averaging the fractal dimension found for each individual image in the set. To avoid the pixel padding skewing results, the processed plume images are cropped to a starting resolution of 512 pixels by 512 pixels before they are box counted.

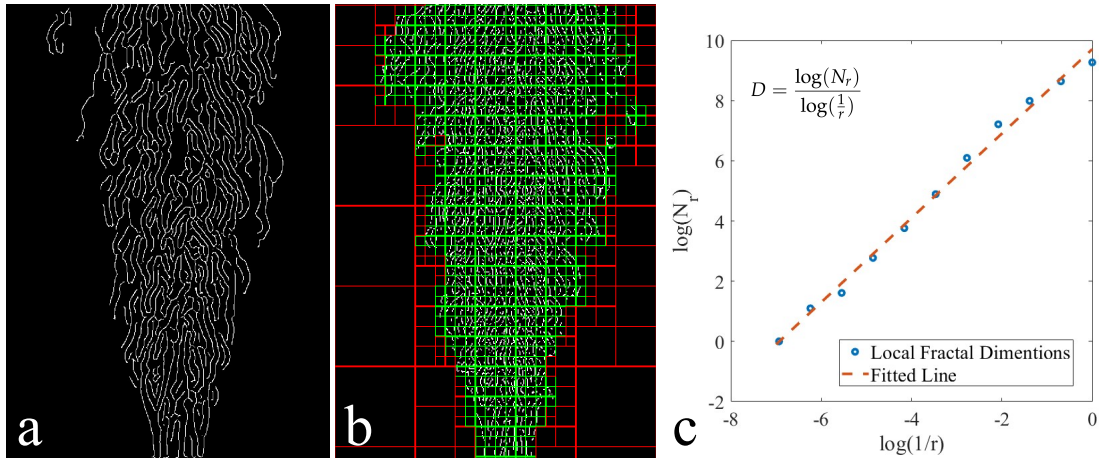


Figure 3.3: (a) A binary image of turbulent ($Re = 1985$) plume edges on which (b) box counting is visually demonstrated and a (c) plot of the log of the number of counted boxes (N_r) versus the log of one over box size in pixels ($1/r$) for the image shown.

The effect of resolution on the accuracy of box counting was analyzed using the singular high resolution (4024 pixels by 6048 pixels) schlieren/shadowgraphy images. The high resolution images were analyzed to determine the impact that starting resolution had on the output fractal dimension. This was accomplished by first processing a singular high resolution image at its native resolution of 4024 by 6048 pixels, then cropping it to a starting resolution of 3200 by 3200 pixels. The

image was first box counted at the starting resolution, then down-sampled to a resolution that was one pixel by one pixel smaller using MATLAB's *imresize* function and binarized to maintain contrast. The image was then processed through the box counting algorithm once again at the new resolution. This process was repeated down to an image resolution of one pixel by one pixel. It was determined that starting resolution did not have a significant impact on the accuracy of fractal dimension until it dropped below 128 by 128 pixels [41].

3.2 Plume Fractal Dimension

Fractal analysis results for the full plume edge detection of schlieren and shadowgraphy images are presented in Figure 3.4. For the regions where laminar behavior was observed, the fractal dimension stays close to one as is expected due to the lack of complexity in laminar behavior. A fractal dimension of 1 corresponds to 1 dimensional behavior, laminar plumes have edges that are straight lines so a fractal dimension of 1 is expected for them. This suggests that cutoffs whose laminar fractal dimension values are at or very close to 1 are more accurate. For transitional plumes, the fractal dimension increases quickly until it levels out at a fractal dimension between 1.4 and 1.5 for turbulent plumes. Horizontal cutoff images show an underestimation of fractal dimension at laminar and transitional Reynolds numbers. This behavior is not unexpected because the plume has a vertical density gradient, so regions that are laminar are not observed. A similar underestimation can be seen with circular cutoff at higher Reynolds numbers, as the top of the plume begins to mix out into the surrounding air and the refractive index gradient is not as prominent, a slight underestimation in the fractal dimension is observed due to a loss of plume definition at the top of the plume images. Based on the data gathered, vertical cutoff schlieren and shadowgraph imaging illustrate the complexity of turbulent plumes the best, while also being able to identify the smooth lines produced in laminar flow. This is expected based on these cutoff orientations being best aligned with the refractive disturbance primary gradient direction as recommended for schlieren imaging [3].

For the cutoff methods that were most promising, further image processing was done to extract the edge only images shown in Figure 3.2, the fractal dimensions of these plumes are presented in Figure 3.5. This type of edge detection results in a significantly lower fractal dimension because there is not enough area available for the box counting algorithm to evaluate the images properly. While the fractal dimension is significantly lower, the same trend for laminar to turbulent transition can be observed. However, the laminar results for this type of edge detection do not begin at a value of 1 as would be expected. This suggests that the edge only edge detection produces inaccurate fractal dimension.

For both edge detection methods, there is more fluctuation in the fractal dimension of the transitional region due to the nature of the transitional plumes.

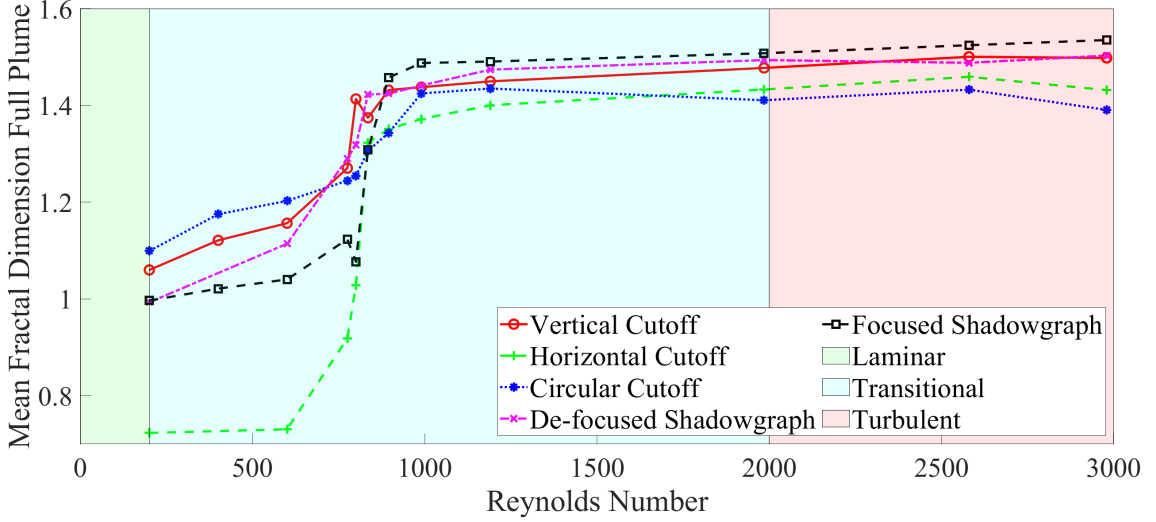


Figure 3.4: Mean fractal dimension of 1000 images vs Re for each cutoff type using full plume edge detection.

Transitional plumes fluctuate between laminar and turbulent behavior consistently, and this causes the noise that is observed between Reynolds numbers of 700 and 1000 in both graphs. The standard deviation between all of the fractal dimensions in each set of images (σ) was found to be low, specific values are presented in Table 3.2. Table 3.2 also shows the average uncertainty in the linear fit used to find the fractal dimension of each image (σ_B). The behavior of the fractal dimension plot is not perfectly linear, so the extent of the uncertainty in the linear fit was found using [42]:

$$\sigma_B = \sqrt{\frac{1}{n_B - 2} \sum_{i=1}^{n_B} \left(y_i - \frac{\sum x^2 \sum y - \sum x \sum xy}{\delta} - \frac{n \sum xy - \sum x \sum y}{\delta} x_i \right)^2} \sqrt{\frac{n_B}{\delta}} \quad (3.1)$$

where

$$\delta = n \sum x^2 - (\sum x)^2 \quad (3.2)$$

Vertical cutoff images have the lowest standard deviation between calculated fractal dimension values, this combined with its ability to depict laminar and turbulent trends accurately, suggests that it is the best choice of cutoff for this application. The vertical cutoff performs best here because the cutoff is oriented to visualize the direction with the largest refractive index gradient, which yields the qualitatively best schlieren image [3].

The histogram distribution of fractal dimension within the thousand image sets for each Reynolds number in the vertical cutoff is shown in Figure 3.6. The evolution from laminar to turbulent fractal dimension is illustrated there. The ranges of the laminar and turbulent distributions are relatively narrow, while

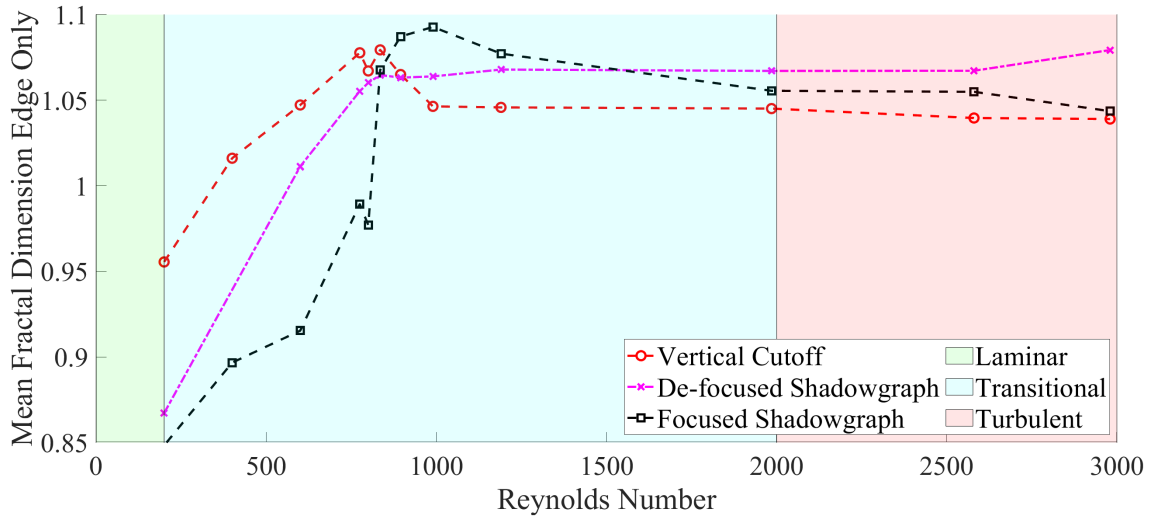


Figure 3.5: Mean fractal dimension of 1000 images vs Re for select cutoff types using edge only edge detection.

the transitional distributions are more widespread and have less of a Gaussian behavior. With more resolution at the transitional flows it may be possible to resolve the effects of intermittency on the fractal dimension which would likely show a bimodal distribution, with one spike that would be more laminar and one that would be more turbulent.

The fractal dimension of transitional plumes also increases with distance from the pipe exit. Figure 3.7 shows the fractal dimension of three representative transitional plumes for vertical cutoff and both types of shadowgraphy. Regions in the images that are observably turbulent reflect turbulent fractal dimension, and laminar regions reflect laminar fractal dimensions. For the whole image the fractal dimension yields an intermediate value between the laminar and turbulent values based on the relative presence of laminar versus turbulent regions.

Table 3.2: Standard deviations of fractal dimension in 1000 image sets for select cutoffs and Reynolds numbers, as well as mean uncertainty in the linear fit to find fractal dimension for each image in the set.

Cutoff type	Re	σ		σ_B	
		Edge only	Full plume	Edge only	Full plume
vertical cutoff	200	0.011	0.014	0.0454	0.0546
	800	0.018	0.018	0.0936	0.1264
	2980	0.008	0.007	0.0999	0.1063
focused shadowgraph	200	0.031	0.031	0.0519	0.0448
	800	0.013	0.026	0.0473	0.0517
	2980	0.010	0.123	0.1144	0.0976
de-focused shadowgraph	200	0.057	0.080	0.0599	0.084
	800	0.031	0.037	0.0773	0.1064
	2980	0.010	0.012	0.1025	0.1142

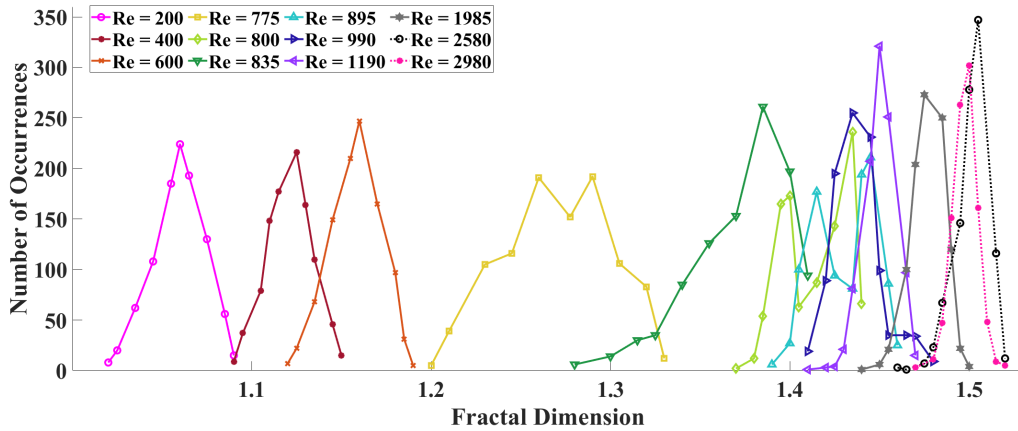


Figure 3.6: Histogram distribution of fractal dimension for each flow rate in the vertical cutoff. Each flow has 1000 images processed.

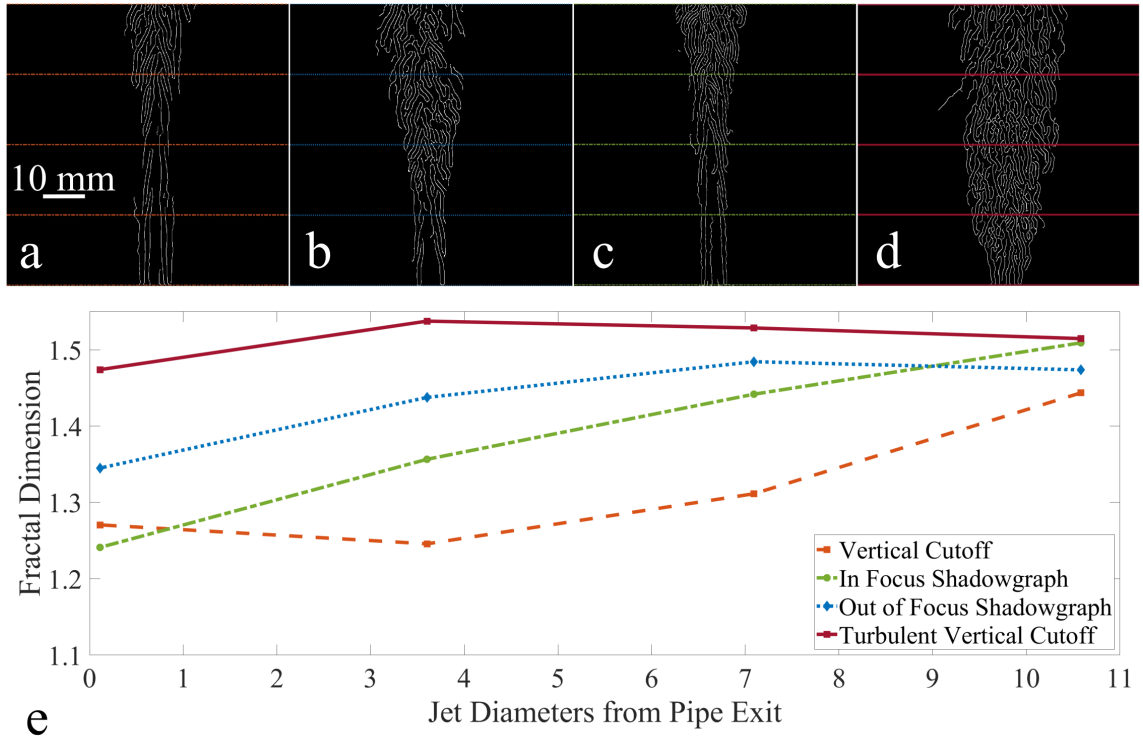


Figure 3.7: Edge detection of transitional plumes with Reynolds number = 835 (a) vertical cutoff (whole image $D = 1.3516$) (b) de-focused shadowgraph (whole image $D = 1.4182$) (c) focused shadowgraph (whole image $D = 1.3960$) (d) Graph showing the variation of fractal dimension along the plume length. (e) Graph showing the variation of fractal dimension along the plume length.

CHAPTER 4

LIMITS OF DETECTION FOR BOS IMAGES

The limits of detection for BOS are analyzed for the application of building leak detection where a projected background and a laser speckle background are compared to a printed background to determine their efficacy. Both Horn-Schunck optical flow and the wavelet optical flow analysis (wOFA) approach developed by Schmidt [32] are used for processing to determine which resolves turbulent flows more effectively. Each background type is imaged at b/L values of 0.035, 0.1, 0.2, 0.3, 0.4, and 0.5 to determine the minimum b/L distance at which it is possible to detect plumes in the BOS system.

4.1 Limits of plume detection for BOS

Figure 4.1 shows raw images of each BOS background type, from these it is apparent that the projected and laser speckle backgrounds have significantly less contrast than the printed background, which is not ideal for BOS as it makes pixel shifts more difficult to track. Figure 4.2 shows individual images of plumes processed using the Horn-Schunck method of optical flow for each tested b/L value and background type. Printed BOS clearly visualizes the plume for each b/L value down to the minimum of 0.035. The projected background only shows the plume clearly for $b/L = 0.3$ and $b/L = 0.5$. The laser speckle background begins to lose fidelity below a b/L of 0.3, but retains more fidelity than the projected background. Due to the use of a low-powered laser, the laser illumination was not uniform from the top of the BOS images to the bottom, so a loss of resolution can be seen near the top edge of the laser speckle plumes where laser light became dimmer.

For both projected and laser speckle backgrounds, the background pattern is visible in processed images even with larger b/L values, i.e. 0.4 and 0.5. This may be due to a slight shifting in the backgrounds while recording, or simply the fact that the observed pixel shifts from the projected backgrounds are smaller overall, so the error in the Horn-Schunck optical flow code is more significant by comparison. The decreased shift in the projected backgrounds may be due to the lack of contrast in the projected and laser speckle backgrounds impacting the Horn-Schunck processing.

Figure 4.3 shows individual images of plumes processed using wOFA, it is evident that this approach yields significantly cleaner results compared to the Horn-Schunck approach. Once again, the printed background resolves the plume at each b/L distance, but for this processing method, the laser speckle background resolves the plume at each b/L distance as well. The projected background shows promising results for b/L values down to 0.3, but loses almost all fidelity below that, solidifying the idea that the projected background is less effective than the printed or laser speckle backgrounds. This is likely due to the fact that the projector had a fan for cooling, which slightly shook the background during testing. The projected background also had less contrast than the printed background and blurrier edges than the laser speckle background, likely making it more difficult for the optical flow codes to track pixels. It should also be noted that for both processing methods the plume shape that is resolved does not look as intricate as may be expected for turbulent flow, this is likely due to a smearing effect caused by long exposure times.

In order to quantify how effective each BOS background was at each b/L value for both processing methods, the average observed pixel shift was calculated. When averaging the pixel shift observed in the image, only the portion of the image where the plume was expected to be was analyzed. The area of the image where there was no flow was used to determine a baseline "flow off pixel shift" as a way to quantify the error present in the optical flow code. Figure 4.4 shows the section of the image that was used for averaging for the flow off and flow on areas of the image. Each of these regions were manually selected on the images. Mean pixel shifts were found by averaging the pixel shift values in the area of interest for both flow on and flow off portions of the BOS images. To obtain an overall average pixel shift for the background and flow rate combination, the average pixel shift of the background was subtracted from the average pixel shift for the flow on area of the image.

The projected and laser speckle backgrounds were projected through the plumes from above and to the left, so that if a shadowgraph effect occurred in the image it would appear on the lower right side of the image. To avoid this skewing the results, the right side of the images was not taken into account when determining the average pixel shift.

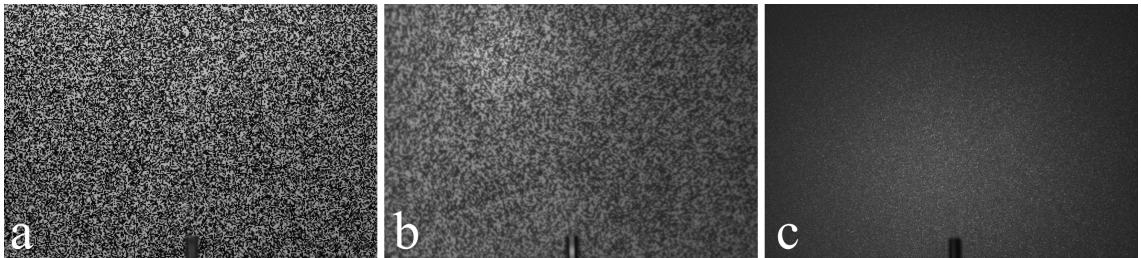


Figure 4.1: Raw BOS images of each background type: (a) printed, (b) projected, and (c) laser speckle, all with a b/L value of 0.4.

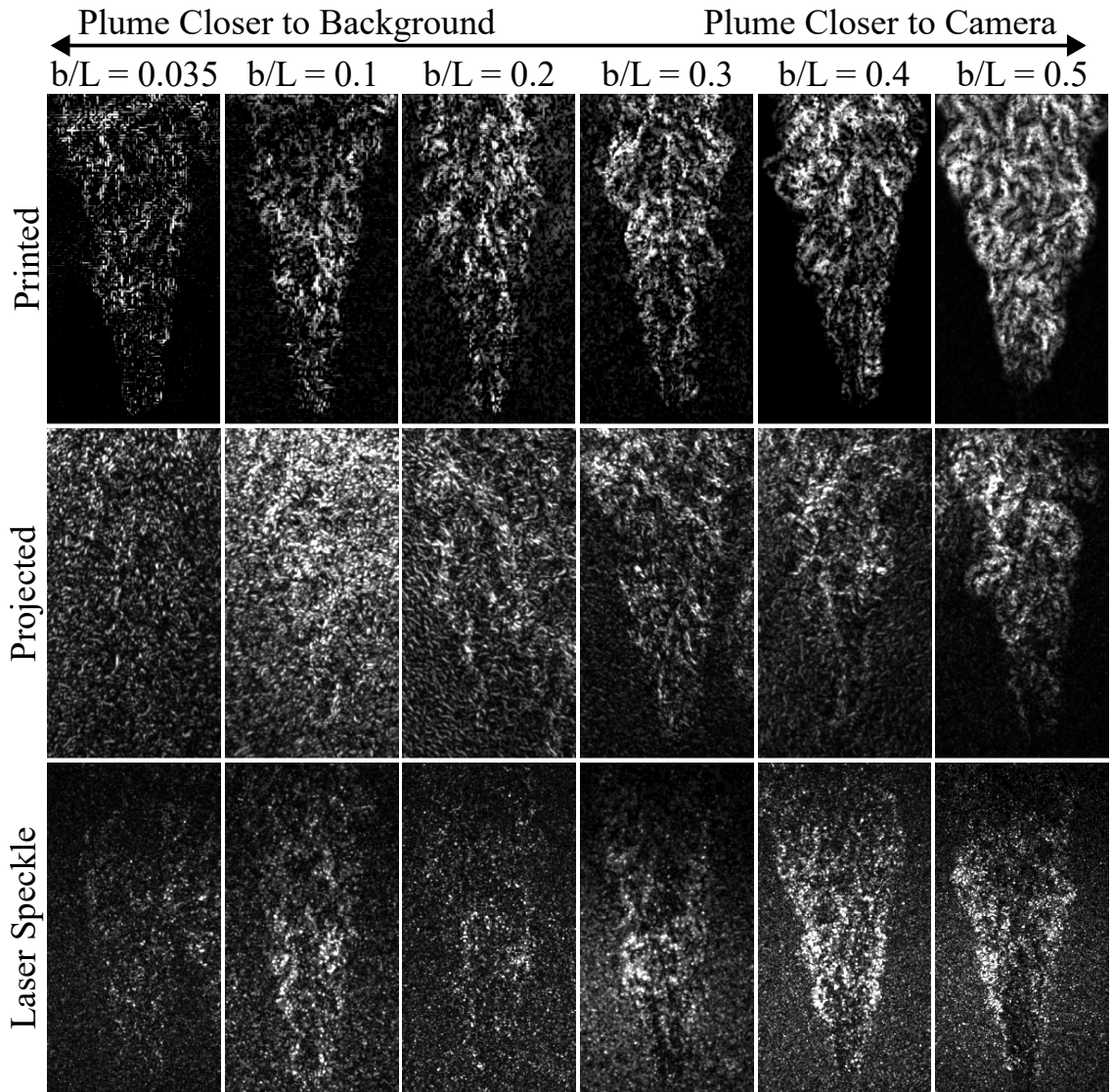


Figure 4.2: Singular BOS images processed using Horn-Schunck optical flow for each combination of background and b/L distance, with $Re = 1985$.

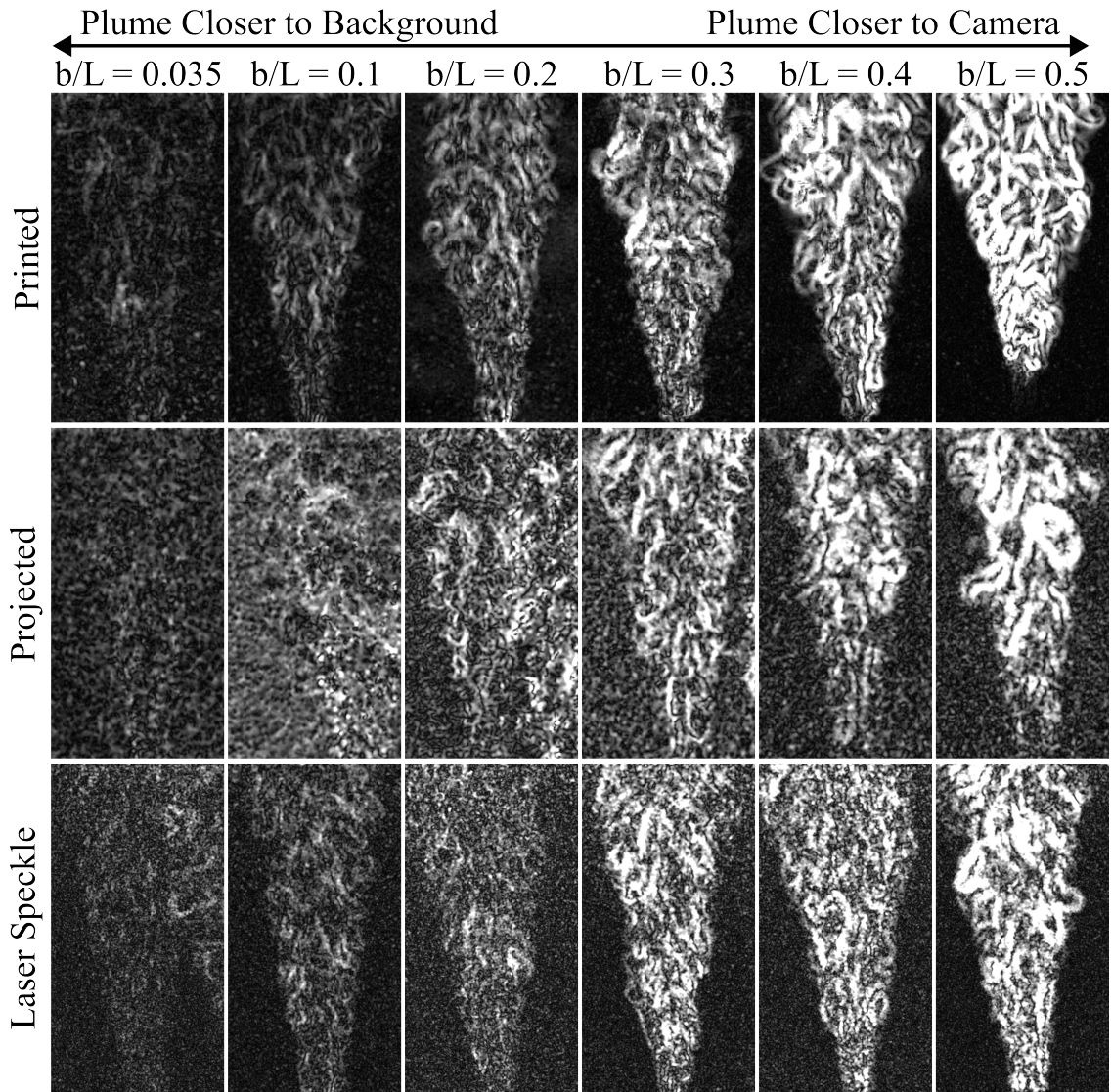


Figure 4.3: Singular BOS images processed using the wOFA approach for each combination of background and b/L distance, with $Re = 1985$

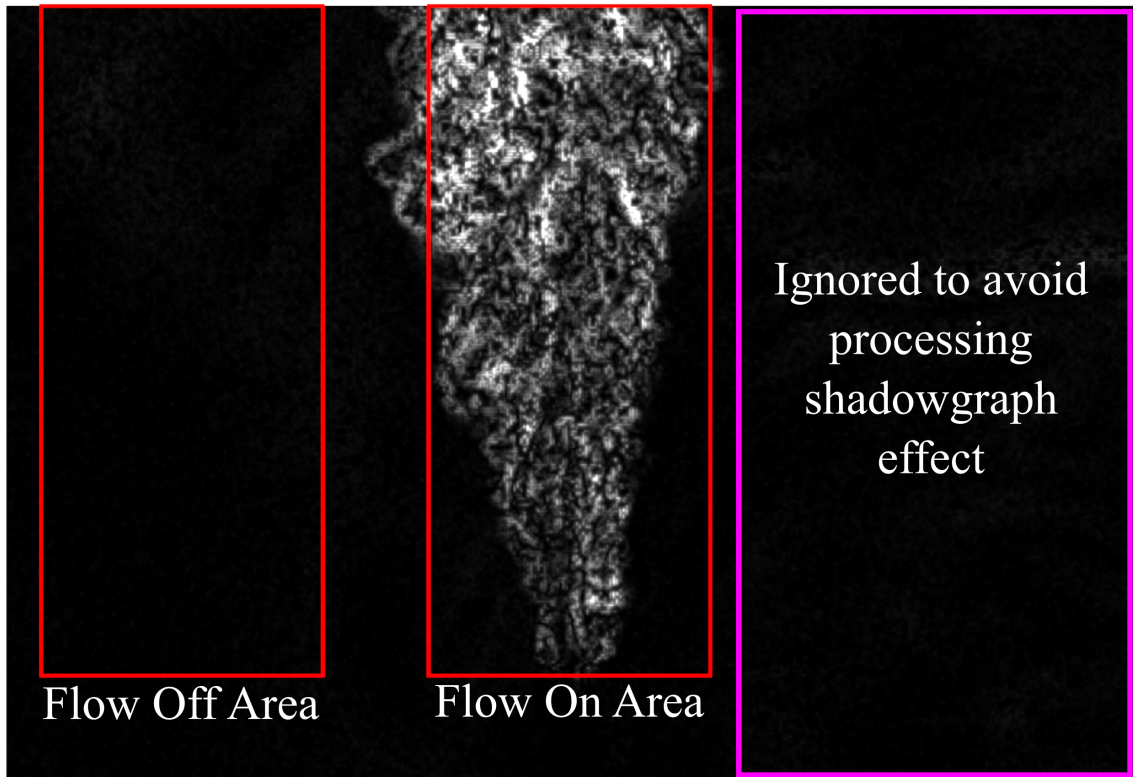


Figure 4.4: Depiction of the areas averaged in each BOS image to determine average pixel shift, showing a plume imaged with a b/L of 0.4 against printed background and processed using Horn-Schunck optical flow.

For the images shown in Figures 4.2 and 4.3, average pixel shifts for both flow on and flow off portions of the images were determined. These are graphed in Figures 4.5 through 4.9. Ideally the average pixel shift should increase as b/L increases until the camera loses significant focus for either the event or the background because increasing b/L increases the sensitivity of a BOS system, thus increasing the observed pixel shift in the system [14]. For a good BOS system, it would also be expected that the flow on pixel shift should be significantly higher than the flow off pixel shift so that in processed images it is possible to distinguish the event from the image background.

Figure 4.5 shows the average flow on pixel shift for the Horn-Schunck processed BOS images compared to the average flow off shift. It is evident that the printed background is the most effective BOS background, because the flow off pixel shift is lower than the pixel shift observed in the plume for every b/L distance; at a b/L of 0.035 the values do become very close, which makes sense given that the plume and the background are in almost the same plane in that case. A slight decrease in pixel shift is seen for $b/L = 0.5$, which suggests that that b/L distance may over range the system. The projected background shows the worst results: it has a seemingly random average pixel shift distribution, and the flow off pixel shift for these images is very close to, if not higher than, the flow on pixel shift observed for most b/L cases. The laser speckle background does not show the expected trend of decreasing average pixel shift with decreasing b/L , but the average pixel shift of the plume area of the image remains consistently above the average pixel shift for the background suggesting that it is a viable option for detection, but shows little promise for any sort of quantitative analysis. Figure 4.6 shows the trend for average pixel shift for an individual image when the flow off pixel shift is subtracted from flow on pixel shift to illustrate average pixel shift more cleanly. Note that both Figure 4.5 and Figure 4.6 are graphed with a log scale for the y-axis due to the variation in scales between pixel shift for varying background types. For Figure 4.6, all negative pixel shift values are marked on the x-axis of the plot.

Figure 4.7 depicts the average pixel shifts for the plumes processed using the wOFA code. The trends seen here are far more expected for a BOS system. The printed BOS background shows an ideal linear increase in pixel shift with increasing b/L , and consistent flow off pixel shift over all b/L values. This suggests that the wOFA code is a superior processing method. The projected background still shows noisy results, and has an instance of negative overall pixel shift at a b/L of 0.1, so even with better processing the projected background is not very ideal. The laser speckle background has noisy results, but never a negative overall pixel shift, and trends similarly to the projected background suggesting that it may be a viable alternative background for the application of building leak detection. Figure 4.8 shows the trend of average pixel shift when flow off pixel shift is subtracted from flow on pixel shift, note that when processed using the wOFA approach all backgrounds share the same order of magnitude for baseline background pixel shift.

Figure 4.9 compares the average overall pixel shift for processing using both

Horn-Schunck and wOFA while plotting the negative values for both cases on the x-axis. In this figure it is clear that wOFA processing has higher and more consistent pixel shift values, fewer negative overall pixel shifts, and a more linear increasing trend with increasing pixel shift, making wOFA the ideal processing method for this data in terms of pixel shift. Figure 4.10 displays two processed BOS images, both with a b/L of 0.3, and imaged against a laser speckle background, one image is processed using Horn-Schunck optical flow, and one using wOFA, this figure demonstrates that wOFA is clearly superior for resolving the plume visually in processed images.

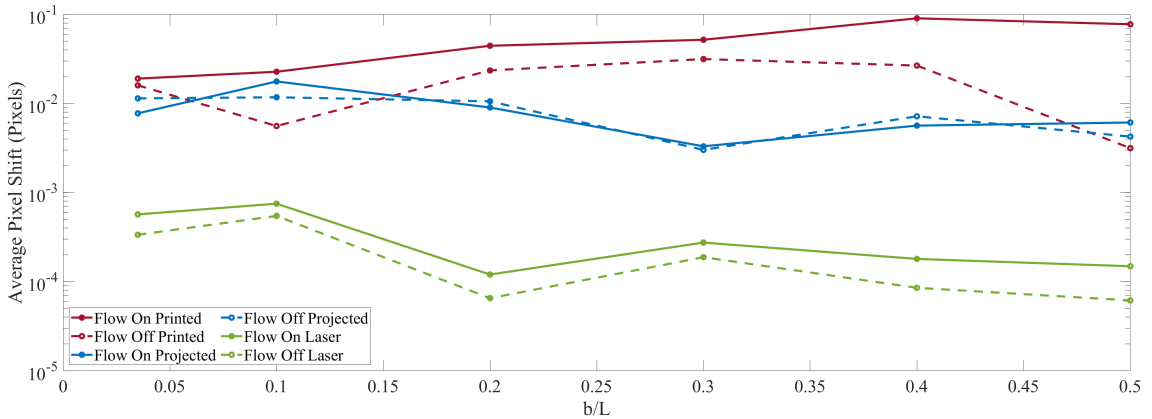


Figure 4.5: The average pixel shift in the flow on area of singular BOS images processed with Horn-Schunck optical flow plotted against the flow off pixel shift for the same image for each background type at each b/L value. Larger pixel shifts indicate more sensitivity and ability to visualize the plume.

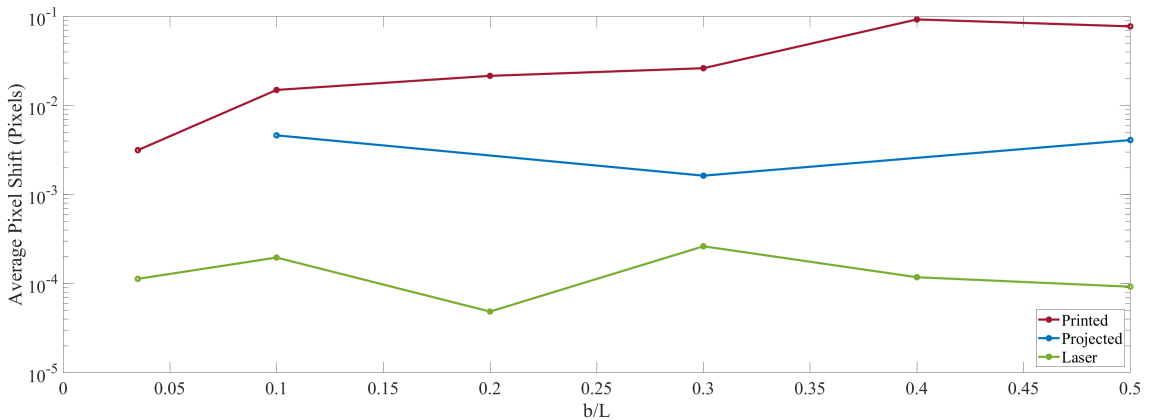


Figure 4.6: The average pixel shift for singular BOS images processed with Horn-Schunck optical flow with the flow off pixel shift subtracted at each b/L , where negative values for the projected background are marked on the x-axis of the plot.

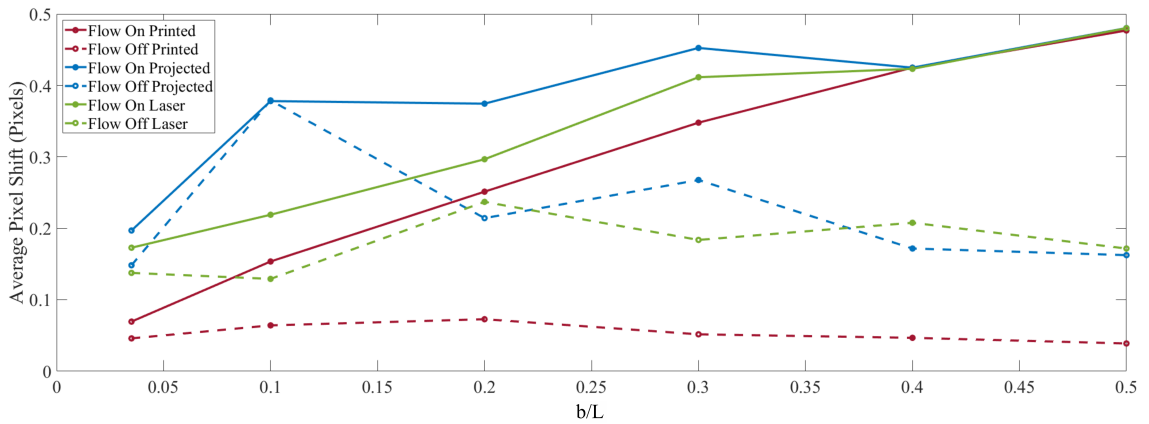


Figure 4.7: The average pixel shift in the flow on area of singular BOS images processed with wOFA plotted against the flow off pixel shift for the same image for each background type at each b/L value.

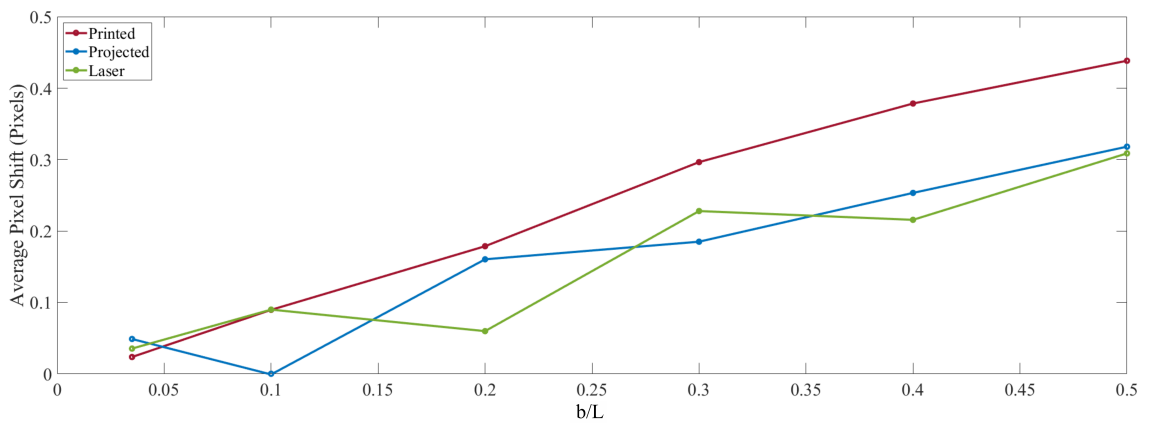


Figure 4.8: The average pixel shift for singular BOS images processed with wOFA with the flow off pixel shift subtracted at each b/L .

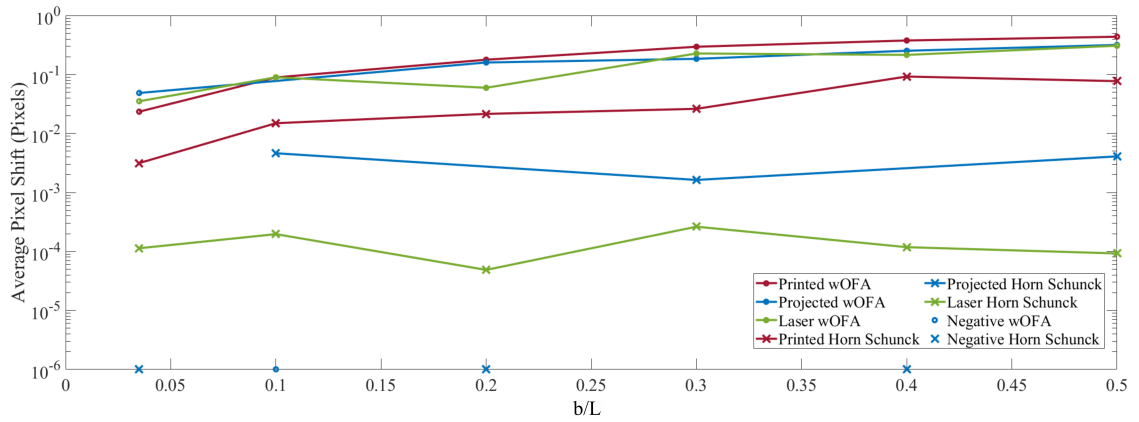


Figure 4.9: The average pixel shift for singular BOS images processed with Horn-Schunck optical flow compared to the same images processed with wOFA, both with the flow off pixel shift subtracted at each b/L value, where negative values for the projected background are marked on the x-axis of the plot.

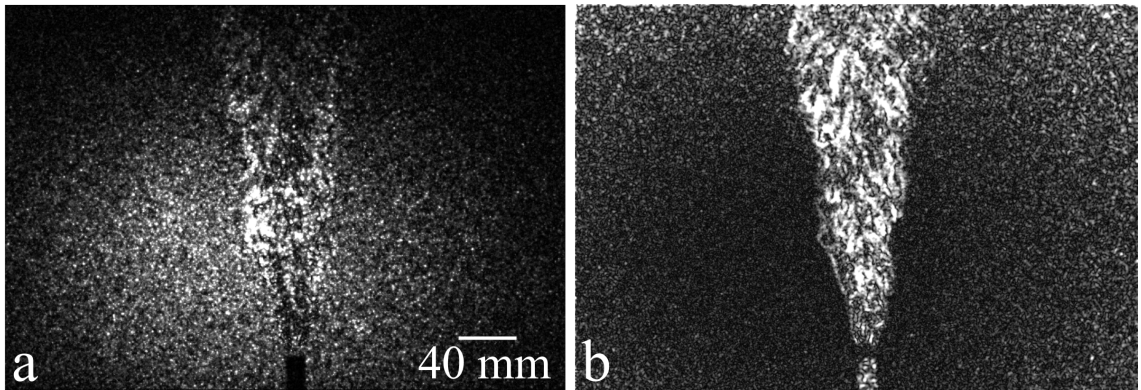


Figure 4.10: Comparison of a BOS image taken with a b/L of 0.3 using the laser speckle background processed using (a) Horn-Schunck optical flow, and (b) wOFA

While the wOFA approach is more accurate it required significantly more processing time per image, the Horn-Schunck method takes about 8.7 seconds to process a single image, and wOFA takes about 345 seconds, which is about 40 times longer. In an attempt to improve the noisier results from the Horn-Schunck method, all fifty of the images taken in the BOS system were processed using the Horn-Schunck method, and averaged to create an average BOS image. These averaged images are shown in Figure 4.11, this process was found to be ineffective, because it blurs the edges of well defined plumes, and increases background noise where it is present. The averaged images for higher b/L values still return a relative shape, but background noise becomes visible for almost every test case, and plume shape becomes less apparent.

The average pixel shifts were also calculated from the averaged images across all fifty of the images in an attempt to improve the trends seen in the pixel shift graphs. These pixel shifts are presented in Figures 4.12 and 4.13. Figure 4.13 shows a more expected trend for the printed background pixel shifts with b/L continuing to increase, however the pixel shift remaining relatively constant for a b/L of 0.1 through 0.3 is unexpected. The trends for the projected and laser speckle backgrounds remain consistent from the analysis of singular BOS images. This further supports the idea that a wavelet based optical flow approach is the ideal BOS processing for these turbulent images.

The wavelet based approach reconstructs the plume shapes so well, that these processed singular images were run through the full plume edge detection code that was used for the schlieren images to determine if edges could be extracted for more information about the BOS plumes. These results are shown in Figure 4.14. Plumes imaged against the printed and laser speckle backgrounds are reasonably reconstructed using this edge detection with b/L ranging from 0.1 to 0.5, but not at the minimum b/L . Projected plumes do not provide enough resolution to effectively recreate their edges with Canny edge detection at any background distance. For Canny edge detection a σ_c value of four was used, and the threshold values for each background and b/L combination are listed in Table 4.1.

Table 4.1: Threshold (T) values used for the MATLAB *edge* function based on background type and b/L value for full plume edge detection

b/L	0.035	0.1	0.2	0.3	0.4	0.5
Printed	0.15	0.15	0.15	0.15	0.25	0.32
Projected	0.29	0.27	0.27	0.35	0.35	0.4
Laser	0.3	0.4	0.35	0.35	0.35	0.35

A larger increase in pixel shift as background distance increases indicates a more sensitive BOS system. For the graphs presented in Figures 4.5, 4.7, and 4.12 the linear slopes were calculated for each background type and method and are presented in Table 4.2, and visualized in Figures 4.15, 4.16, and 4.17. Steeper slopes of linear fit lines correspond to more sensitive BOS systems. Negative

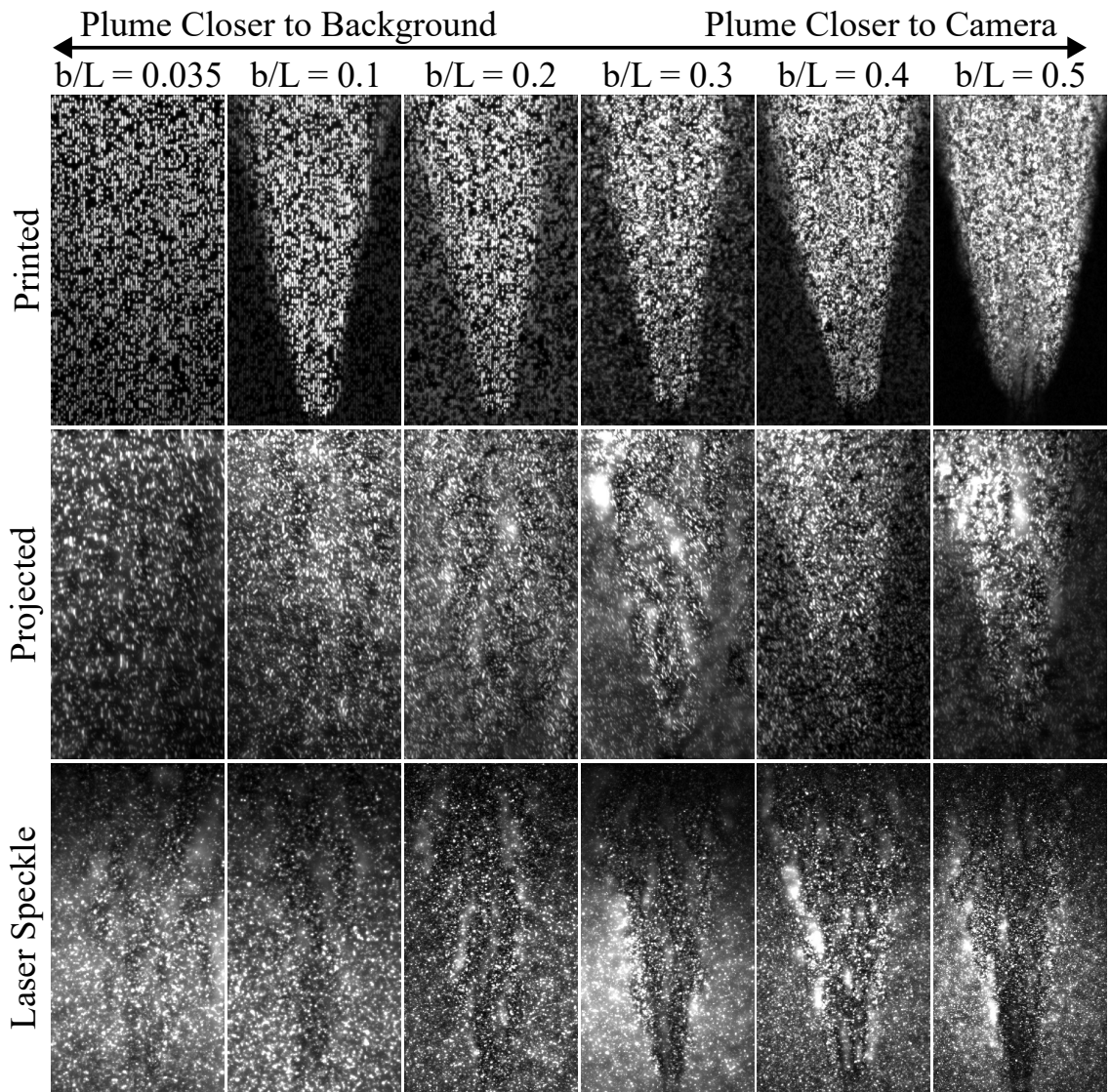


Figure 4.11: Averaged BOS images processed using Horn-Schunck optical flow for each combination of background and b/L distance, with $Re = 1985$.

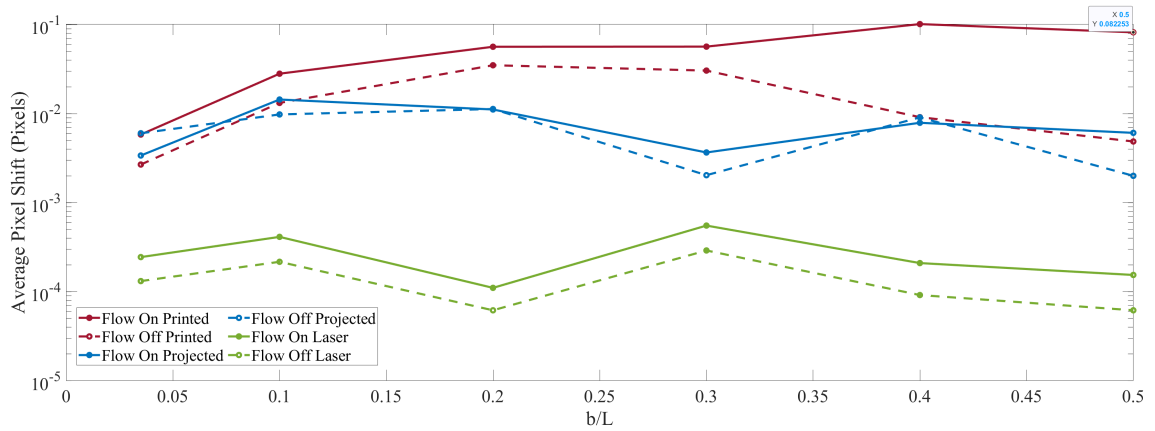


Figure 4.12: average pixel shifts for the flow on portion of fifty BOS images processed using Horn-Schunck optical flow plotted against the average pixel shift for the flow off portion of those images, for each background type and b/L combination.

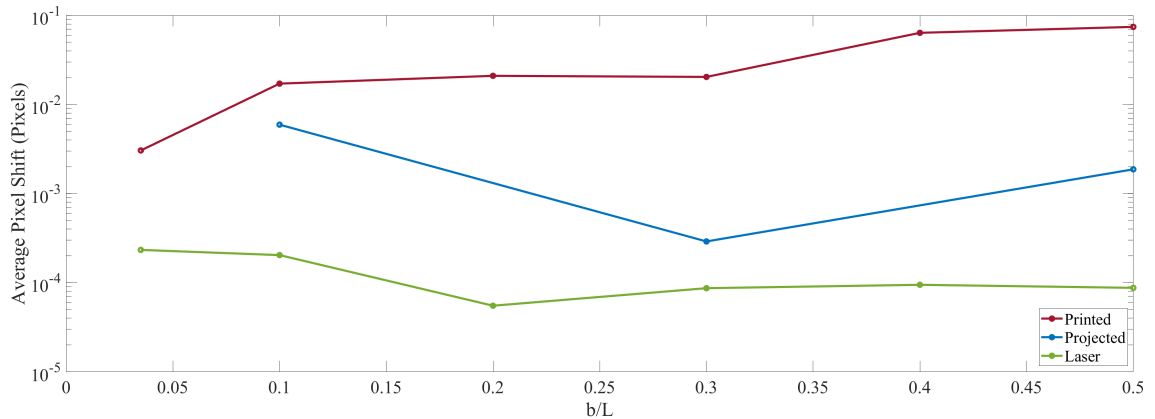


Figure 4.13: average pixel shifts for the flow on portion of fifty BOS images processed using Horn-Schunck optical flow with the average pixel shift for the flow off portion of those images subtracted, for each background type and b/L combination, where negative values for the projected background are ignored.

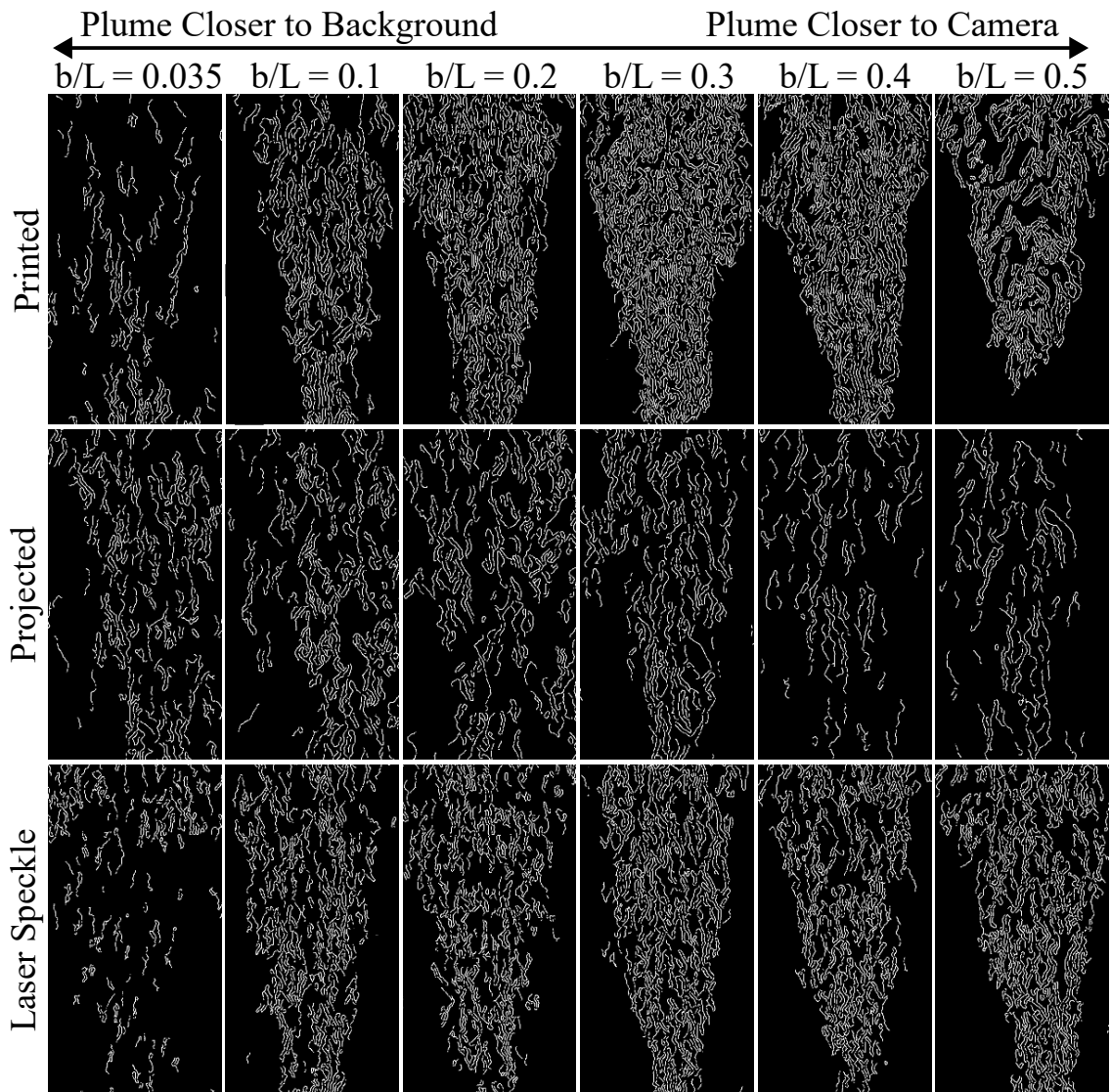


Figure 4.14: Full plume edge detection applied to BOS images processed using wOFA.

Table 4.2: Slopes of linear fit lines for each processing method and background type combination when average flow on pixel shifts are subtracted from average flow off pixel shifts

Processing Method	Background Type	Slope of Linear Fit
wOFA	Printed	0.8826
	Projected	0.4747
	Laser Speckle	0.6791
Horn-Schunck: Single Image	Printed	0.1793
	Projected	-0.0052
	Laser Speckle	$-2.037 \cdot 10^{-5}$
Horn-Schunck: Average Image	Printed	0.1517
	Projected	-0.0159
	Laser Speckle	-0.0011

slopes were found for the projected and laser speckle backgrounds when using Horn-Schunck processing for both single and average images, indicating that this processing method is not viable for projected backgrounds. All of the slopes found for wOFA pixel shift lines were positive and reasonable, further indicating that this method was more effective at resolving the plumes captured in the BOS images. For wOFA processing, the printed background has the highest slope indicating it is the most sensitive, the laser speckle background is the second most sensitive, and the projected background was the least sensitive.

Ultimately, the printed and laser speckle backgrounds showed the most promising results for BOS background, and wOFA provided the best analysis. For the application of building leak detection, a light and portable BOS system is needed, making laser speckle backgrounds an optimal choice. For a well set up BOS system using wOFA, plume resolution is retained down to a minimum b/L value of 0.035, and the ability to reconstruct plume edges from a BOS image is retained down to a b/L value of 0.1, which supports that a BOS system with a projected laser speckle background is feasible for the application of building leak detection.

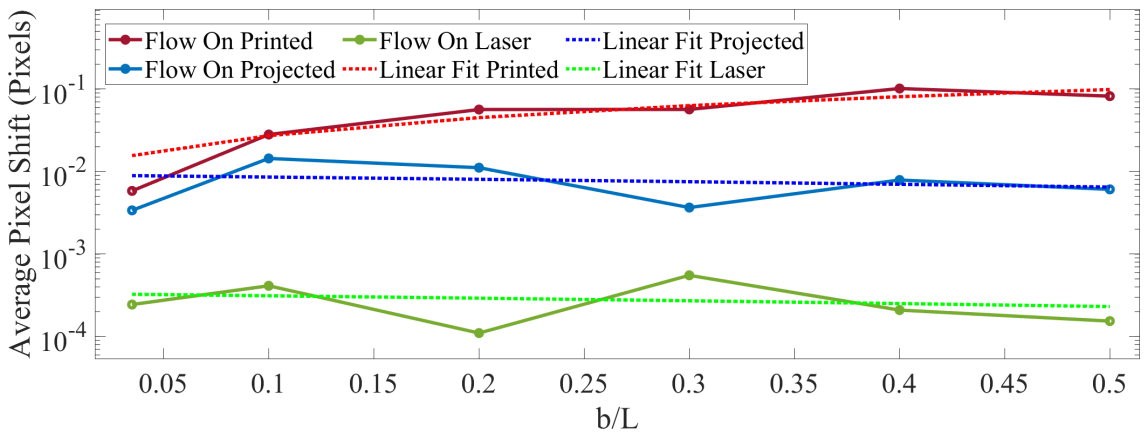


Figure 4.15: The average pixel shift in the flow on area of singular BOS images processed with Horn-Schunck optical flow plotted against the linear fit for the same data at each b/L value. Steeper slopes indicate more sensitivity and ability to visualize the plume.

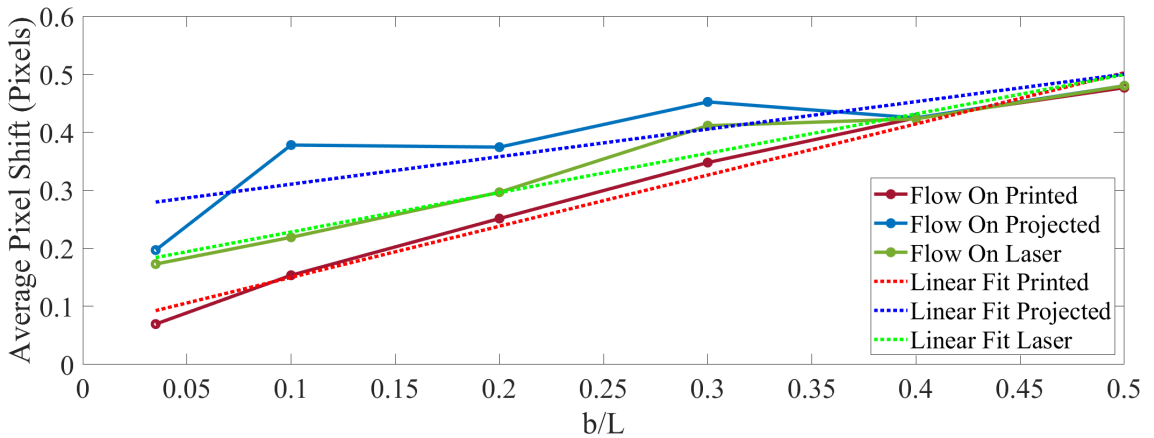


Figure 4.16: The average pixel shift in the flow on area of singular BOS images processed with wOFA plotted against the linear fit for the same data at each b/L value. Steeper slopes indicate more sensitivity and ability to visualize the plume.

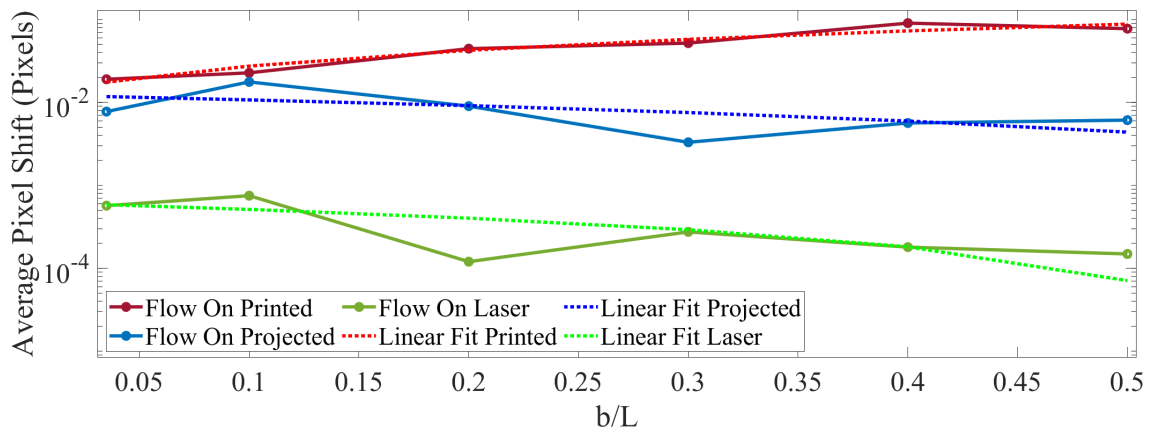


Figure 4.17: The average pixel shifts for the flow on portion of fifty BOS images processed using Horn-Schunck optical flow plotted against the linear fit for the same data, for each background type and b/L combination. Steeper slopes indicate more sensitivity and ability to visualize the plume.

CHAPTER 5

CONCLUSIONS AND FUTURE WORK

5.1 Conclusions

A trend of increasing fractal dimension with increasing jet Reynolds number was observed in schlieren and shadowgraph images of helium plumes transitioning from laminar to turbulent flow. Shadowgraph and vertical cutoff schlieren visualized the details of turbulence most accurately for qualitative imaging and yielded the most consistent results from the image processing used to find fractal dimension. Vertical cutoff images resulted in the lowest standard deviation of calculated fractal dimension suggesting that this cutoff type was ideal for this case, which is not unexpected due to the orientation of the primary refractive index gradient in the vertically aligned plume. The fractal dimension of the turbulent helium plumes was found to be between 1.4 and 1.5, while laminar plumes had a fractal dimension between 1 and 1.1, depending on cutoff. With the vertical cutoff, the fractal dimension was found to be 1.05 ± 0.1 for laminar flow and 1.48 ± 0.1 for turbulent flow, suggesting that a fractal dimension greater than 1.45 corresponds to fully developed turbulence. Based on previously published values, this method seems to result in a slight overestimation of fractal dimension in turbulence but may still be useful in determining physical properties of plumes, including flow regime. Transitional plumes that exhibit behaviors seen in both laminar and turbulent plumes are shown to have an intermediate fractal dimension value, with the fractal dimension varying along the plume length. The fractal dimension increases along the plume as it transitions from laminar to turbulent in the ambient environment.

The laser speckle background was found to be the best projected background alternative to the printed background for the application of building leak detection. This background outperformed the projected background for detecting pixel shifts and reconstructing plume images when processed. The projected background provided noisy results, which can either be attributed to the shaking of the background caused by the projector's cooling fan, the lack of contrast in the background, or a combination of the two. The wOFA approach for BOS processing outperformed the Horn-Schunck method of optical flow, it resulted in higher and more consistent pixel shifts that had lower background error when compared to overall pixel shift. When processed using wOFA, both printed and laser speckle backgrounds were found to retain qualitative resolution down to a

the minimum tested b/L value of 0.035, and the ability to detect edges in these images was retained down to a b/L value of 0.1.

For future implementations of BOS systems used for detecting building leaks, it is recommended that a projected laser speckle background be used because it is light weight, portable, and produces results comparable to BOS with a printed background so long as wOFA is used for analysis. For future analysis it may be possible to implement the fractal analysis shown for schlieren images to obtain Reynolds number/flow regime data for detected building leaks. A BOS system mounted to a drone may be feasible for building examination to locate leakage, to accomplish this it is recommended that both the camera and the laser projection are well-mounted to the drone to compensate for jitter, and shift correction should be used for the wOFA analysis to account for this as well.

5.2 Future Work

Future experiments should be conducted to better reflect real world conditions. Rather than helium, turbulent plumes of air with a temperature difference from the ambient air should be imaged to more accurately simulate building leakage. More backgrounds can be explored for this application, particularly the use of building textures as explored by Boudreaux [1], would be helpful for eliminating the need to insert backgrounds when performing building leak detection. These experiments may also explore the feasibility of performing experiments at night so that contrast from the laser speckle background is greater outdoors, and in an effort to increase the temperature difference between indoors and outdoors. It may also be interesting to look into the effects of humidity on schlieren systems, and if a difference in humidity between indoors and outdoors increases or decreases the sensitivity of BOS for this application. Ultimately a BOS system will need to be tested while mounted from a drone to determine if the drone movement impacts results.

Changes could be made to both the laser speckle and projected backgrounds to improve BOS results. For laser speckle backgrounds, a higher powered laser should be used to ensure more even illumination and better contrast in outdoor environments. If projected backgrounds are further explored, a higher quality projector should be used to reduce movement introduced from the cooling fan and increase the contrast of the projected pattern. Future experiments may also benefit from affixing the laser or projector to the camera so that when the background shifts the camera does as well, so the background remains stationary from the camera's perspective. Because it is not possible to obtain a true background image for building leakage, it may be possible to create "synthetic background images", or capture an image of how the background pattern should look for certain images, similar to the work explored by Weisberger and Bathel (2022) [18].

If it is possible to reasonably resolve the edges of plumes imaged using BOS, the next logical step is to apply box-counting to these plumes so that their fractal dimension can be related a Reynolds number or flow regime. There may be issues

resolving more laminar or low Reynolds number flows with BOS because of the lack of variation in these plumes, especially with the lack of a flow off background image. Fractal analysis may offer a method of determining at what approximate Reynolds number resolution is lost for BOS detected leakage plumes.

REFERENCES

- [1] Philip Boudreaux, Singanallur Venkatakrishnan, Emishaw Iffa, and Diana Hun. Application of reference-free natural background-oriented schlieren photography for visualizing leakage sites in building walls. *Building and Environment*, 223:109529, 2022.
- [2] Ralph T. Muehleisen, Kasanthamy Chelliah, Hirenkumar Patel, and Ganesh Raman. Modifying nearfield acoustic holography for use in building leak detection. *Journal of the Acoustical Society of America*, 139(4):2109–2109, 2016.
- [3] G. S. Settles. *Schlieren and Shadowgraph Techniques*. Springer, 2006.
- [4] T B Fisher, M K Quinn, and K L Smith. An experimental sensitivity comparison of the schlieren and background-oriented schlieren techniques applied to hypersonic flow. *Measurement Science and Technology*, 30(6):065202, 2019.
- [5] Amayu W. Gena, Conrad Voelker, and Gary S. Settles. Qualitative and quantitative schlieren optical measurement of the human thermal plume. *Indoor Air*, 30(4):757–766, 2020.
- [6] Michael J. Hargather and Gary S. Settles. A comparison of three quantitative schlieren techniques. *Optics and Lasers in Engineering*, 50(1):8–17, 2012.
- [7] Jesse D. Tobin and Michael J. Hargather. Quantitative schlieren measurement of explosively-driven shock wave density, temperature, and pressure profiles. *Propellants, Explosives, Pyrotechnics*, 41(6):1050–1059, 2016.
- [8] Michael J. Hargather and Gary S. Settles. Retroreflective shadowgraph technique for large-scale flow visualization. *Applied Optics*, 48(22):4449, 2009.
- [9] Frank Austin Mier and Michael J. Hargather. Color gradient background-oriented schlieren imaging. *Experiments in Fluids*, 57(6), 2016.
- [10] Erik Goldhahn and Jörg Seume. The background oriented schlieren technique: sensitivity, accuracy, resolution and application to a three-dimensional density field. *Experiments in Fluids*, 43(2–3):241–249, 2007.
- [11] Florian Herbst, Melf Peters, and Joerg Seume. To the limits of the application of the BOS method. In *11th International Conference on Fluid Control, Measurements and Visualization*, 2011.

- [12] Mateo Gomez, Samuel J. Grauer, Josh Ludwigsen, Adam M. Steinberg, Steven F. Son, Sukesh Roy, and Terrence R. Meyer. Megahertz-rate background-oriented schlieren tomography in post-detonation blasts. *Applied Optics*, 61(10):2444, 2022.
- [13] Markus Raffel, Nathaniel T Smith, C Christian Wolf, James T Heineck, and Anthony D Gardner. Projected moving patterns for reference-free background-oriented schlieren technique (BOS). *Measurement Science and Technology*, 35(11):115306, 2024.
- [14] M. J. Hargather. Background-oriented schlieren diagnostics for large-scale explosive testing. *Shock Waves*, 23(5):529–536, 2013.
- [15] Lia Becher, Conrad Voelker, Volker Rodehorst, and Michael Kuhne. Background-oriented schlieren technique for two-dimensional visualization of convective indoor air flows. *Optics and Lasers in Engineering*, 134:106282, 2020.
- [16] Junhao Rong, Yanqiu Huang, Yihang Zhao, Yi Wang, Xin Li, Junwei Guo, Wenyang Wang, and Shengnan Guo. A novel measurement for evaluating the capture efficiency of local ventilation system using background oriented schlieren. *Building and Environment*, 267:112185, 2025.
- [17] Zhen Lyu, Weiwei Cai, and Yingzheng Liu. An event-triggered background-oriented schlieren technique combined with dynamic projection using dynamic mirror device. *Measurement Science and Technology*, 35(10):105302, 2024.
- [18] Joshua M. Weisberger and Brett F. Bathel. Projection background-oriented schlieren. *Applied Optics*, 61(20):6006, 2022.
- [19] Markus Raffel. Background-oriented schlieren (BOS) techniques. *Experiments in Fluids*, 56(3), 2015.
- [20] K. R. Sreenivasan. Fractals and multifractals in fluid turbulence. *Annual Review of Fluid Mechanics*, 23(1):539–600, 1991.
- [21] Alex P. Pentland. Fractal-based description of natural scenes. *IEEE Transactions on Pattern Analysis and Machine Intelligence*, PAMI-6(6):661–674, 1984.
- [22] Benoît B. Mandelbrot. *The fractal geometry of nature*. W. H. Freeman, New York, updated and augmented, 18. print. edition, 1982.
- [23] James Theiler. Estimating fractal dimension. *Journal of the Optical Society of America A*, 7(6):1055, 1990.
- [24] Benoit B. Mandelbrot. On the geometry of homogeneous turbulence, with stress on the fractal dimension of the iso-surfaces of scalars. *Journal of Fluid Mechanics*, 72(03):401, 1975.

- [25] Pilar Lopez, Ana M. Tarquis, Ania Matulka, Benjamin Skadden, and José M. Redondo. Multiscaling properties on sequences of turbulent plumes images. *Chaos, Solitons and Fractals*, 105:128–136, 2017.
- [26] R. R. Prasad and K. R. Sreenivasan. Scalar interfaces in digital images of turbulent flows. *Experiments in Fluids*, 7(4):259–264, 1989.
- [27] G. F. Lane-Serff. Investigation of the fractal structure of jets and plumes. *Journal of Fluid Mechanics*, 249(1):521, 1993.
- [28] R. I. Sykes and R. S. Gabruk. Fractal representation of turbulent dispersing plumes. *Journal of Applied Meteorology and Climatology*, 33(6):721 – 732, 1994.
- [29] Haris J. Catrakis and Paul E. Dimotakis. Mixing in turbulent jets: scalar measures and isosurface geometry. *Journal of Fluid Mechanics*, 317:369–406, 1996.
- [30] Bradley Atcheson, Wolfgang Heidrich, and Ivo Ihrke. An evaluation of optical flow algorithms for background oriented schlieren imaging. *Experiments in Fluids*, 46(3):467–476, 2008.
- [31] Berthold K.P. Horn and Brian G. Schunck. Determining optical flow. *Artificial Intelligence*, 17(1–3):185–203, 1981.
- [32] Bryan E. Schmidt and Mark R. Woike. Wavelet-based optical flow analysis for background-oriented schlieren image processing. *AIAA Journal*, pages 1–8, 2021.
- [33] Maurizio Lazzaro and Roberto Ianniello. Corrigendum: Image processing of vaporizing gdi sprays: a new curvature-based approach. *Measurement Science and Technology*, 29(11):119501, 2018.
- [34] Maurizio Lazzaro. Characterization of the liquid phase of vaporizing gdi sprays from schlieren imaging. *Measurement Science and Technology*, 30(8):085401, 2019.
- [35] John Canny. A computational approach to edge detection. *IEEE Transactions on Pattern Analysis and Machine Intelligence*, PAMI-8(6):679–698, 1986.
- [36] Lijun Ding and Ardeshir Goshtasby. On the Canny edge detector. *Pattern Recognition*, 34:721–725, 2001.
- [37] Rafael C. Gonzalez and Richard E. Woods. *Digital image processing*. Pearson Education, New York, New York, 4th edition, 2018.
- [38] The MathWorks Inc. 2-d fast Fourier transform. The MathWorks Inc., 2024.
- [39] The MathWorks Inc. 2-d inverse fast Fourier transform. The MathWorks Inc., 2024.

- [40] Helge Petersen. The properties of helium: Density, specific heats, viscosity, and thermal conductivity at pressures from 1 to 100 bar and from room temperature to about 1800k. Technical report, Danish Atomic Energy Commission Research Establishment Riso, 1970.
- [41] Maria N. D’Orazio, Christian Peterson, and Michael J. Hargather. Characterization of the fractal dimension of helium plumes in laminar to turbulent transition. *Experiments in Fluids*, 66(4), 2025.
- [42] John R. Taylor. *An introduction to error analysis*. University Science Books, 1997.

APPENDIX A

CODES

A.1 Schlieren Edge Detection Code

```
%Maria D'Orazio
%Detection of fractal edges of turbulent helium plume
%% Clear all
clear all
close all
clc

tic
%% Read in image folder

num = 1001; %number of images to work through
fold = imageDatastore("C:\Users\maria\OneDrive\Documents\Lab\helium
plume\Fractals\Fractal_Images_and_code\20240105_Shadowgraph_InFocus_Tiffs\Shadowgraph_InFocus_150LPM_S0001");%load in folder and read all images
IM = readall(fold);
FD = zeros(num,1);
sigB = zeros(num,1);
THRESH = 0.1;
sig = 4;
x1 = [480 325 750 670];
x2 = [355 335 405 395];
%jx = [575 575 490 490; 575 575 490 490; 575 575 490 490; 575 575 490 490; 575 585 480
490;575 615 450 490;575 685 390 490;575 685 390 490; 575 700 370 490; 575 720 330 490;
575 800 300 490; 575 800 300 490;575 800 280 490;575 800 280 490; 575 800 280 490; 575
800 280 490;595 800 280 470; 595 800 280 470; 595 800 280 470; 595 800 280 470];

%% Image read in

for cnt = 1:num %for loop runs through FD process for all images

B = 12; %Define Bit depth
% file_name = '100LPM_Plume.tif'; %Define file name
file_BG = 'Shadowgraph_InFocus_BG.tif'; %Define background image file name
% Z = double(imread(file_name))./(2^B);
Z = double(IM{cnt})./(2^B); %double(imread('Circular_10_LPM.tif'))./(2^B);
BG = double(imread(file_BG))./(2^B);
z = Z - BG; %imsubtract(Z,BG);
zr = rescale(z);
zrs = zr(70:787,153:870);
% figure (1)
%imshow(zr)
%imwrite(zr,'zz_Background_subtracted_plume.tif')

%% FFT of image setup

% To Create a gradient of image

I = zr; %image to be used for FFT

FI = gradient(I,0.01); %imfilter(imfilter(zr,[1,-2,1]],[1,-2,1]); %gradient(gradient
(zr))
```

```
FIr = rescale(FI);
% figure
% imshow(FIr);
%imwrite(FIr,'zz_Gradient_of_background_subtracted_plume.tif')

f=uint8(FIr.*(2^8)); %reads the image in
[n,m] = size(f); %detmeines the size of the image

F=fft2(f, n*2 ,m*2);%does the FFT (binary image)

s=abs(F); %get rid of negatives bc you cant see them
sn=s/max(max(s));

sa=imadjust(sn, [0 0.01], [0,1]); %histogram strech to see the image frequency better

sas = fftshift(sa);
[r,c] = size(F);

% figure,
%imshow(sas)
%imwrite(sas,'zz_Fourier_transformed_image.tif')

%% Select Filter For FFT

D_0 = 0.1; %turb: 1.5;

%highpass Gaussian
H_hf = zeros(r,c);
N = 2;
for k = 1:1:r
    for l = 1:1:c

        D(k,l) = (((k - (r/2))^2) + ((l - (c/2))^2))^(1/2);
        H_hf(k,l) = (1 - exp(-(D(k,l))^2/(2*D_0^2)));

    end
end

% figure
% imshow(H_hf)
%imwrite(H_hf,'zz_highpass_Gaussian_filter_D0_0.1.tif')

% %highpass butterworth
% H_hf = zeros(r,c);
% for k = 1:1:r
%     for l = 1:1:c
```

```

%
%      D(k,l) = (((k - (r/2))^2) + ((l - (c/2))^2))^(1/2);
%      H_hf(k,l) = 1/(1+(D_0./(D(k,l))).^2*N);
%
%      end
% end
%% Put Image back to normal

Fs = fftshift(F);

HH = H_hf.*Fs;

Gs = fftshift(HH);
g = ifft2(Gs);
gu = (real(g(1:n,1:m)));
G8 = uint8(gu);
G8R = rescale(G8);

% figure,
%imshow(G8R, [])
%imwrite(G8R, 'zz_Image_through_gaussian_filter_D0_1.5.tif')

%% Canny Method

threshold = [0, THRESH]; %edit the settings for the canny filter
sigma = sig;
BWc = edge(G8R, 'canny', threshold, sigma);
% figure
%imshow(BWc)
% title('Binary Gradient Mask')
%imwrite(BWc, 'zz_Image_With_Canny_edge.tif')

%% Get rid of edge

MIN = 400; %restraints on im find circles
MAX = 500;
S = 0.98;
SUB = 15;
% [cen,rad] = imfindcircles(BWc, [min,max], 'Sensitivity', S);
cen = [536.02, 527.52];
rad = 487;
%imshow(BWc)
%viscircles(cen, rad);
CM = drawcircle('Center', cen, 'Radius', rad-SUB, 'visible', 'off'); %create mask to delete
circle and everything outside of it
BWCM = createMask(CM, BWc);
% figure
% imshow(BWCM)

NOC = BWc.*BWCM;
% figure

```

```
% imshow(NOC)

%% Get rid of noise

x =x1; %20: [575 490 490 575]; %50: [290 480 570 750]; %100: [480 290 800 600]; vertices ✓
of trapazoid shape that noise will be deleted outside of
y = [900 130 130 900];
TM = roipoly(NOC,x,y);

% figure
% imshow(TM)

TMN = NOC.*TM;

TMN_b =TMN(130:900,175:945);

% figure
% imshow(TMN)
%imwrite(TMN,'zz_Image_With_Noise_Removed.tif')

%% Show me whats happening
ign = TMN+zr;
% figure
% imshow(ign)
% figure
% imshow(zr)
%imwrite(ign,'zz_Image_over_BGsuborig.tif')

%% Isolate outer edge
[row,col] = find(TMN_b); %create matrix of all "1" pixels in TMN
RC = [row,col];
NEW = TMN_b; %set up a duplicate of our edge picture

middle = 360; %define middle collumn of picture
coll = find(col==middle);
midedge = round(coll(1));

AP = 40; %Area around pixel
rightint = zeros(length(row),AP);
pf = 0.01;

for i = 1:midedge
for j = 1:AP
    v = TMN_b(row(i),(col(i)-j));
    rightint(i,j) = v;
end
end

pain = mean(rightint,2);
```

```
for i = 1:length(pain)
if pain(i) > pf
    NEW(row(i),col(i)) = TMN_b(row(i),col(i))*0;
end
end

for i = midedge:length(row)
for j = 1:AP
    v = TMN_b(row(i),(col(i)+j));
    rightint(i,j) = v;
end
end

pain = mean(rightint,2);

for i = 1:length(pain)
if pain(i) > pf
    NEW(row(i),col(i)) = TMN_b(row(i),col(i))*0;
end
end

% figure
% imshow(NEW)
%imwrite(NEW,'zz_Attempt_at_middle_removal_4.tif')
% figure
% imshow(NEW+zr)
%imwrite(NEW+zr,'zz_Best_Image_so_far_5.tif')

%% top
%
pft = 0.00;
APt = 2;
topint = zeros(APt,length(col));
NEWt = TMN;

for i = 1:length(col)
for j = 1:APt
    v = TMN(row(i)+j,(col(i)));
    topint(j,i) = v;
end
end

paint = mean(topint,1);

for i = 1:length(paint)
if paint(i) > pft
    NEWt(row(i),col(i)) = TMN(row(i),col(i))*0;
end
end
```

```

FIN = NEWt+NEW;

% figure
% imshow(NEWt)

c = NEWt+NEW;

% figure
% imshow(c)
% imwrite(c,'100LPM_OutterEdge.tif')

% figure
% imshow(c+zr)
% imwrite(FIN,'zz_better.tif')
% imwrite(c+zr,'100LPM_OutlineonPlume.tif')
%

%% Remove noise again
%
GOD = NEW;

%xs = [360 320 440 400]; %20: [520 545 545 520];%50: [505 560 630 450]; %100: [485 575
660 400];
y2 = length(TMN_b);
y = [y2 0 0 y2];
TMG = roipoly(GOD,x2,y);
% figure
% imshow(TMG)
TMT = imcomplement(TMG);
TMNT = GOD.*TMT;
% TMN_b = TMNT(70:787,153:870);
[Nr,r] = boxcount(TMNT);
LNR = log(Nr);
LR = log((1./r));
p = polyfit(LR,LNR,1);
FD(cnt) = p(1);

sigb = 0;
N_sig = size(LR,2);
delta = N_sig.*(sum(LR.^2)) - (sum(LR)).^2;
for sigi = 1:N_sig
    sigb_c = sqrt((1./(N_sig-2)).*(LNR(sig_i) - ((sum((LR.^2)).*sum(LNR)) - (sum(LR).*sum
((LR.*LNR)))))./(delta) - ((N_sig.*sum(LR.*LNR) - sum(LR).*sum(LNR))./delta).*LR(sig_i)).^2).
*sqrt(N_sig./delta);
    sigb = sigb + sigb_c;
end

sigB(cnt) = sigb;

disp(cnt)

```

```
% figure
% imshow(TMNT)
% imwrite(TMNT,'42LPM_OutterEdge.tif')
% figure
% imshow(TMNT+zr)
% imwrite(TMNT+zr,'42LPM_OutlineonPlume.tif')
```

end

toc

A.2 Horn-Schunck Optical Flow Code and Functions

```
% Maria D'Orazio
% HSOF AVG

%% Clear
clear all
close all
clc

%% Define Variables
N = 50;
B = 8;
filepath = "C:\Users\maria\Desktop\HE_BOS_02202025\T29";
bg_file = "C:\Users\maria\Desktop\HE_BOS_02202025\T29\T29-03062025123837-0.tiff";
TestNum = 'T29_';
xres = 2200;
yres = 3208;

%% HSOF
bg = double(imread(bg_file))./(2^B);
bg = bg(:, :, 1);
C = cellac(N,B,filepath);
[uOut,vOut] = HSOF(bg,C);

%% avg of imgs

avgau = zeros(xres,yres);
avgav = zeros(xres,yres);

writematrix(abs(uOut{2}), append('singimu_',TestNum))
writematrix(abs(vOut{2}), append('singimv_',TestNum))

% figure; imshow(rescale(abs(uOut{2})));
% figure; imshow(rescale(abs(vOut{2})));

for j = 10:10:N

    avgau = zeros(xres,yres);
    avgav = zeros(xres,yres);

    for i = 2:j
        us = abs(uOut{i} - uOut{i-1});
        vs = abs(vOut{i} - vOut{i-1});
        avgau = avgau + us;
        avgav = avgav + vs;
    end

    avgu = avgau./j;
    avgv = avgav./j;

    writematrix(avgv, append('avgv_',TestNum, num2str(j)))
```

```
writematrix(avgu, append('avgv_', TestNum, num2str(j)))

% figure; imshow(rescale(avgu));
% figure; imshow(rescale(avgv));
end

avgtot = rescale((avgu+avgv)./2);
figure; imshow(avgtot);
```

```
function [uOut,vOut] = HSOF(coldIm,images,inputs,guess)
%% Summary
% Computes the HSOF solution between a cold image and a series of hot
% images.

%% Inputs
% coldIm - The image with no deflection.
% images - The series of images with deflection, saved as a cell array
% inputs - Controls for HS, in the format of a struct with subsets tol,
% pxpmm, alpha, and maxIteration.

%% Parse Inputs
[Ny,Nx] = size(coldIm);

switch nargin
    case 1
        error('Both cold and hot images are required')
    case 2
        tol = 0.00008;
        pxpmm = 1;
        alpha = 1;
        maxIteration = 100;
        u = zeros(Ny,Nx);
        v = zeros(Ny,Nx);
    case 3
        tol = inputs.tol;
        pxpmm = inputs.pxpmm;
        alpha = inputs.alpha;
        maxIteration = inputs.maxIteration;
        u = zeros(Ny,Nx);
        v = zeros(Ny,Nx);
    case 4
        tol = inputs.tol;
        pxpmm = inputs.pxpmm;
        alpha = inputs.alpha;
        maxIteration = inputs.maxIteration;
        u = guess.u;
        v = guess.v;
end

%% Initialize Variables

uOut = cell(length(images),1);
vOut = cell(length(images),1);

%% Solving
for i = 1:(length(images))
    tic

    % Make the intensity gradient matrix E
    [Ex,Ey,Et] = buildE(coldIm,images{i}(:, :, 1));
```

```
% Initialize iteration parameters.
iter = 0;
err = 1;
while max(max(err)) >= tol
    iter = iter+1;
    % Build the average u and v matrices
    [uBar,vBar] = buildbar(u,v);

    % Solve the iterative equation
    uNew = uBar - ( Ex.*((Ex.*uBar)+(Ey.*vBar)+Et))./(alpha^2+Ex.^2+Ey.^2);
    vNew = vBar - ( Ey.*((Ex.*uBar)+(Ey.*vBar)+Et))./(alpha^2+Ex.^2+Ey.^2);

    % Calculate convergence criteria
    err = sqrt((uNew-u).^2+(vNew-v).^2);

    % Update guesses
    u = uNew;
    v = vNew;
    if iter > maxIteration
        % End if max number of iterations mets
        break
    end
    if mod(iter,10) == 0
        % Update console feedback
        disp(['Iteration: ',num2str(iter)])
        disp(['Error: ',num2str(max(max(err)))]])
    end
end
end
% Initialize new guess
u = uNew;
v = vNew;

% Save out converged results
uOut{i} = u/pxpmm;
vOut{i} = v/pxpmm;
disp(i);
toc
end

end
```

```
function [uBar,vBar] = buildbar(u,v)
%% Summary
% Laplacian filtering
h = [1/12 1/6 1/12;...
     1/6 0 1/6;...
     1/12 1/6 1/12];
[n,m] = size(u);

uBar = conv2(u,h,'same');
vBar = conv2(v,h,'same');

end
```

```
function [Ex,Ey,Et] = buildE(im1,im2)
%% Summary
% Builds the brightness partial derivatives.
Ex = conv2(im1,0.25* [-1 1; -1 1], 'same') + conv2(im2, 0.25*[-1 1; -1 1], 'same');
Ey = conv2(im1, 0.25*[-1 -1; 1 1], 'same') + conv2(im2, 0.25*[-1 -1; 1 1], 'same');
Et = conv2(im1, 0.25*ones(2), 'same') + conv2(im2, -0.25*ones(2), 'same');

end
```

```
function C = cellac(N,B,filepath)

S = dir(fullfile(filepath, '*.tiff'));
imgs = {S.name};
C = cell(N,1);

for k = 1:N
    im = imread(fullfile(filepath, double(imgs{k})));
    im1 = im(:,:,1);
    imdif = double(im1) ./ (2^B);
    C{k} = imdif;
end

end
```

APPENDIX B

PERMISSIONS

Portions of Chapter 2, Chapter 3, and Chapter 4 are reproduced from D’Orazio, M.N., Peterson, C. and Hargather, M.J. Characterization of the fractal dimension of helium plumes in laminar to turbulent transition. *Exp Fluids* 66, 70 (2025), with the permission of Springer Nature: <http://creativecommons.org/licenses/by/4.0>.

PLUME IDENTIFICATION AND ANALYSIS
USING SCHLIEREN AND BACKGROUND ORIENTED SCHLIEREN

by

Maria N. D'Orazio

Permission to make digital or hard copies of all or part of this work for personal or classroom use is granted without fee provided that copies are not made or distributed for profit or commercial advantage and that copies bear this notice and the full citation on the last page. To copy otherwise, to republish, to post on servers or to redistribute to lists, requires prior specific permission and may require a fee.

